The Basal Friction Coefficient of Granular Flows With and Without Excess Pore Pressure: Implications for Pyroclastic Density Currents, Water-Rich Debris Flows, and Rock and Submarine Avalanches

Eric C. P. Breard, Josef Dufek, Luke Fullard, Alexandre Carrara

HAL Id: insu-03594466
https://insu.hal.science/insu-03594466

Submitted on 17 Mar 2022

Key Points:
- The basal friction coefficient is not a constant and a function of nondimensional slip
- A modified Navier slip law could be defined on a given roughness and imply that the shear rate scales with force fluctuations
- Descriptions of shear stresses need to account for the excess pore pressure and predict shear stresses never vanish when shear is present

Correspondence to:
E. C. P. Breard,
ebreard@uoregon.edu

The Basal Friction Coefficient of Granular Flows With and Without Excess Pore Pressure: Implications for Pyroclastic Density Currents, Water-Rich Debris Flows, and Rock and Submarine Avalanches

Eric C. P. Breard[1] , Josef Dufek[1] , Luke Fullard[2] , and Alexandre Carrara[3]

[1]Department of Earth Sciences, University of Oregon, Eugene, OR, USA, [2]School of Food and Advanced Technology, Massey University, Palmerston North, New Zealand, [3]Institut des Sciences de la Terre, University Grenoble Alpes, Université Savoie Mont Blanc, CNRS, IRD, IFSTTAR, Grenoble, France

Abstract Numerous large-scale geophysical flows propagate with low-apparent basal friction coefficients, but the source of such phenomenology is poorly known. Motivated by scarce basal friction data from natural flows, we use numerical methods to investigate the interaction of granular flows with their substrate under idealized conditions. Here we investigate 3-D monodisperse and polydisperse fluid-particle granular flow rheology and flow-substrate interaction using discrete element modeling and coarse-graining techniques. This combination allows us to calculate the continuum fields of solid fraction, velocity, shear stress, and solid pressure and compare it with force measurements on the substrate. We show that the wall/basal friction coefficient is not constant. Instead, it is a function of the nondimensional slip defined as the ratio of the slip velocity over the slip velocity fluctuations. The scaling of the wall friction with nondimensional slip is independent of air viscosity and density and presence of excess pore pressure. Therefore, the reduction of the basal stress that must occur in mobile natural flows with excess pore pressure is not ascribed to the lowering of wall friction coefficient. Instead, lowering of the normal stress by fluid drag in flows with elevated pore fluid pressure justifies the definition of effective wall and internal friction coefficients to capture the geophysical flow rheology and the forcing on its substrate. These results are fundamental to understand the dynamics of geophysical mass flows including pyroclastic density currents, water-rich debris flows, and rock and submarine avalanches.

1. Introduction

Many studies have shown that geophysical mass flows such as volcanic and nonvolcanic landslides, rock avalanches, and concentrated pyroclastic density currents have enhanced mobility, which are often assessed by the well-known mobility index: length of runout/drop height (L/H) (Corominas, 1996; Legros, 2002; Ogburn et al., 2014; Schneider et al., 2010). Plots of L/H against the bulk volume for all mass flows generally depict a positive relationship (increased mobility with volume), which has been attributed to the lowering of the effective bulk friction coefficients.

In the past decades, the quest to find the universal mechanism responsible for the friction reduction in long-runout landslides has motivated many workers to propose a variety of mechanisms that include riding atop a cushion of trapped air (Shreve, 1968), lubrication by water (Lucchitta, 1987), a basal melt layer (Erismann, 1979), frictionally warmed ice (Singer et al., 2012), frictional velocity weakening (Lucas et al., 2014), a basal layer of colliding grains (Campbell, 1989; Cleary & Campbell, 1993), sustained pore pressure (Iverson, 2005; Iverson et al., 1997, 2010), acoustic fluidization (Collins & Melosh, 2003; Johnson et al., 2016; Melosh, 1979), and moisture fluidization and thermal pressurization by frictional heating (Alonso et al., 2016; Goren & Aharonov, 2007; Vardoulakis, 2000; Voight & Faust, 1982; Wang et al., 2017). Nevertheless, compelling evidence for the low effective friction of long-runout mass flows does not imply a universal mechanism precisely because this measure averages over a large range of microphysical processes. Interestingly, a similar conundrum has confounded the pyroclastic flows community for decades (Hayashi & Self, 1992; Kelfoun, 2011; Lube et al., 2019; Wilson, 1980). Notably, for both debris flows and pyroclastic

density currents, large L/H require lowering of the effective basal friction coefficient as noted in many depth-averaged studies (e.g., Charbonnier & Gertisser, 2009; Charbonnier et al., 2013; Lucas et al., 2014; Ogburn & Calder, 2017) or even in discrete element modeling (Borykov et al., 2019). Phenomenologically and mathematically, the low effective basal (also called wall) friction can be produced by either lowering the effective normal stress or reducing the friction coefficient for both landslides and pyroclastic density currents (Breard et al., 2017; Pudasaini & Miller, 2013). This poses the following fundamental question for individual currents: Is the lowering of the basal shear stress a result of the reduction of normal stress, basal friction coefficient, or both? Deciphering which frictional properties need to be modified cannot be accomplished through continuum or depth-averaged approaches as only the net impact of friction reduction is evaluated through a comparison to observations. Yet, the exact physical mechanism influencing these forces is needed to better understand emergent phenomena in natural flows and has implications for deposition, sorting, and internal forces in these flows.

Despite recent advances in the theoretical description of granular flows (Andreotti et al., 2013; Forterre & Pouliquen, 2008; Henann & Kamrin, 2013), there is a need for a better understanding of the interactions between the moving granular material and its interaction with a solid boundary (wall friction) and the resulting rheology of the system. Importantly, the occurrence of nonzero velocity of particles at the base of a flow moving atop a substrate is called slip. The scaling of the slip velocity remains challenging whereas the formation of slip in mass flows is at the origin of substrate entrainment and subsequent bulking (Bernard et al., 2014; Roche et al., 2013), which has been correlated to momentum amplification and subsequent enhanced flow mobility when pore pressure can develop in the substrate (Iverson et al., 2010). Basal slip can generate Kelvin-Helmholtz instabilities that can modify material entrainment from the substrate into the flow (Pollock et al., 2019; Roche et al., 2013).

In order to understand the scaling of slip velocity with other flow properties, measurements of slip velocity, basal forces, and their distribution are required. However, obtaining such data from natural settings remains extremely challenging because of the scale and hazards associated with those systems. In the past decade, our understanding of geophysical mass flows' behavior has been driven by studies of simplified granular systems. Therefore, we turn toward granular mechanics to further our understanding of natural granular flows even though these systems are significantly simpler than natural flows. A number of developments in granular physics have led to a reassessment of the common modeling approach of treating solid interfaces as a simple no-slip boundary condition, even for smooth, frictional vertical walls, which are treated instead with a partial slip boundary condition (Artoni & Richard, 2015). In fact, the existence of cooperative effects (Pouliquen, 2004; Staron, 2008) in the force network and in the velocity field can impede the use of a purely local approach, that is, an approach where local stresses scale to the local shear rate. An important source of cooperative effects and thus of nonlocality is self-generated velocity fluctuations within the flow, which has been simulated in continuum approaches using the fluidity approach (Kamrin, 2017; Kamrin & Koval, 2012), the kinetic theory (Jenkins & Berzi, 2010; Lun et al., 1984) and the Cosserat continuum (Cosserat & Cosserat, 1909; De Borst, 1991).

Here, by means of 3-D discrete element simulations coupled to a state-of-the-art coarse-graining (CG) technique for mono and polydisperse systems, we study simultaneously flow rheology and effective basal friction of granular material on inclined slopes and in a numerical approximation of Couette shear cells. The numerical approach used intentionally simply geophysical cases, yet yield insights into fundamental processes that shape these currents. First, we present the flow rheology for monodisperse and slightly polydisperse beds. Second, we describe the scaling of the wall friction and slip velocity on flat frictional surfaces. Third, we look at the role of roughness on the wall friction and slip velocity. Finally, we investigate the role of normal stress reduction by pore pressure diffusion on the flow rheology and the interactions with its substrate. In this CFD-DEM study, we consider both gas-particle mixtures and the impact of denser, more viscous fluid, in the case of water-particle mixtures.

2. Methods

We use discrete element method (DEM) simulations to assess the rheology of a granular bed while simultaneously measuring the time-variant forces imposed by the bed. The numerical experiments are presented in section section 2.1. The equations of the DEM used in the MFIX model can be found in Garg et al. (2012) and

Benyahia et al. (2012). The CG method applied to polydisperse systems and calculations of the parameters needed to define granular flow rheology is new to the granular physics and Earth science fields and, thus, described thoroughly in section 2.2.

2.1. Discrete Element Modeling

Numerical. simulations were carried out in 3-D with the MFIX-DEM code developed by the U.S. Department of Energy (http://mfix.netl.doe.gov). Details about the theory and implementation of the model can be found in Garg et al. (2012), Syamlal (1998), and Syamlal et al. (2016) and validation of the DEM approaches in Garg et al. (2012) and Li et al. (2012).

The computational domain was a cuboid of length $L_x = L_z = 20$ times the max particle diameters and variable L_y. The X and Z boundaries were made cyclic, whereas the bottom and top walls were either made flat frictional of rough.

The coupling between the particles and the Eulerian fluid is described by the transfer of momentum between phases ($\overrightarrow{I_f}$), which is achieved via summing the drag force and pressure gradient force of particles located in the computational cell (Garg et al., 2012):

$$\overrightarrow{I_f}(t) = \frac{1}{\nu_{REV}} \sum_{k=1}^{N_k} \overrightarrow{F_D}^{(k)}(t) K_{REV}\left(X_p^{(k)}\right),$$ (1)

where $K_{REV}\left(X_p^{(k)}\right)$ is a generic kernel with compact support that determines the influence of the particle force at $X_p^{(k)}$ on the representative elementary volume, ν_{REV}.

The drag force $\overrightarrow{F_D}^{(k)}$ of the particle residing in the cell k is defined as (Garg et al., 2012)

$$\overrightarrow{F_D}^{(k)}(t) = -\nabla P_f(t)\left(\frac{\pi}{6} d_p^{(k)^3}\right) + \frac{\beta_{fs}^{(k)}(t)}{\left(1 - \varepsilon_f(t)\right)}\left(\frac{\pi}{6} d_p^{(k)^3}\right)\left(\overrightarrow{v_f}(t) - \overrightarrow{v_p}^{(k)}(t)\right),$$ (2)

where P_f is the fluid pressure, d_p is the particle diameter, ε_f is the volume fraction of fluid, and v_f and v_p are the fluid and particle velocities, respectively. To calculate the drag force accurately, the mean fluid phase velocity is interpolated to the particle location. Then, the drag force on each particle is projected on the Eulerian fluid phase grid. The interphase momentum exchange term $\beta_{fs}^{(k)}$ is evaluated via a drag model following Gidaspow (1994):

$$\beta_{fs}^{(k)}(t) = \begin{cases} \frac{3}{4} C_D^{(k)}(t) \dfrac{\rho_f\, \varepsilon_f(t)\left(1 - \varepsilon_f\right)\left\|\overrightarrow{v_f} - \overrightarrow{v_s}^{(k)}\right\|}{d_p^{(k)}} \varepsilon_f^{-2.65}, & \varepsilon_f \geq 0.8 \\[2ex] \dfrac{150\left(1 - \varepsilon_f(t)\right)^2 \eta_f}{\varepsilon_f(t)\, d_p^{(k)}2} + \dfrac{1.75\, \rho_f\left(1 - \varepsilon_f(t)\right)\left\|\overrightarrow{v_f}(t) - \overrightarrow{v_s}^{(k)}(t)\right\|}{d_p^{(k)}}, & \varepsilon_f < 0.8 \end{cases}$$ (3)

with ρ_f as the fluid density. The drag coefficient $C_D^{(k)}$ is calculated as follows (Gidaspow, 1994):

$$C_D^{(k)}(t) = \begin{cases} \dfrac{24}{Re^{(k)}(t)\left(1 + 0.15\, Re^{(k)}(t)^{0.687}\right)}, & Re^{(k)}(t) < 1000 \\[2ex] 0.44 & Re^{(k)}(t) \geq 1000 \end{cases}$$ (4)

The full equations of the DEM-CFD code have been added in the supporting information Tables S1 and S2.

The solid mixture was made of spherical monodisperse (one particle size) or slightly polydisperse mixtures (three particles sizes, $d \pm 0.2d$) with a mean diameter (D43) of 500 microns and 5 mm and a solid density of 2,500 kg/m³. In order to ensure hard collisions between particles and the flat frictional wall, we attributed a particle-particle and particle-wall spring constant $k_n > 10^4 P_s d$ (Zhang & Kamrin, 2017), where P_s is the solid pressure. We set the particle-particle and particle-wall friction coefficients to 0.5, with inelastic collisions

since the normal restitution coefficient ~0.5 for many natural geophysical materials (Dufek et al., 2009). The discrete phase is two way coupled to the Eulerian phase chosen as air or water, which is treated as a compressible fluid at an ambient temperature of 293.15 K. In order to investigate whether air temperature affects our results (by influencing the viscosity and density of the interstitial gas), we have performed simulations on flat frictional and rough substrate at 873.15 K. These represent an upper value of temperature measured within concentrated pyroclastic density currents such as block-and-ash and pumice flows (Benage et al., 2016; Lube et al., 2020; Pensa et al., 2018; Trolese et al., 2018). We thus neglect the possible role of temperature on the particle-particle friction coefficient, stiffness of particles, triggering of flash heating, and thermoplasticity if clay particles are present. The Cartesian grid has a spatial resolution in all three dimensions equal to $2d_{mean}$ (the mean particle diameter), ensuring an accurate coupling description between gas and particles (Bergantz et al., 2015). Note that in DEM-CFD, the Eulerian grid size Δx has to be larger than the maximum particle size and that $\Delta x \in (1.85\ d_{mean}, 2.5\ d_{mean})$ since bed statistics in that range are independent of Δx (Bernard et al., 2017). We used a narrow grain-sized distribution to make sure the drag was as (spatially) resolved as possible while enabling small polydispersity to exist.

The rough surface making the bottom or top plates were made of particles sizes $d_r = 0.95\ \overline{d}_f$, where $\overline{d}$ is the mean particle diameter in the flow. Based on the description of Berzi and Vescovi (2017) adapted for non-monodisperse mixtures, the roughness is measured by the minimum penetration angle ψ defined in radians as

$$sin\ \psi = \frac{d_r + l}{d_r + d_f}, \tag{5}$$

where l is the distance between the edges of particles contributing to the roughness, d_r is the particle diameter in the roughness, and d_f is the particle diameter in the flow. For monodisperse mixtures with a roughness made of a single layer of particles positioned at the same height, the minimum penetration angle is reached for $l = 0$ and gives $\psi = 5\pi/30$. In contrast, particles can penetrate the gaps if $\psi > 10\pi/30$. Instead of using a regular lattice that is not representative of natural system and to prevent crystallization of the particles (particles form a lattice with layer thickness $= d$), we chose to change placement of the particles to obtain three domain-averaged roughnesses $\psi = 6\pi/30, 8\pi/30,$ and $10\pi/30$. These values cover the extreme cases, where particles are closely packed in the roughness versus that where particles are far apart, yet preventing any particle falling through the roughness layer. For $\psi > 10\pi/30$ in the first layer, the particles can interact with a second layer of particles underneath, thus leading to a bed average $\psi < 10\pi/30$.

Simulations are divided in two sets: flat friction and rough. Each is thus subdivided in two subsets, monodisperse or polydisperse. Shear in the bed was either generated by imposing a slope (changing the gravity vector) or by simulating a top rough plate on which we imposed a defined confining force and velocity in the x direction (Figures 1a and 1b). Finally, simulations were carried out either in pseudo-steady state, where changes are applied very slowly relative to the response time of particles to changes of the stresses or in complete steady state (Figure 1c).

From the DEM simulations, particles locations, velocity, and forces are exported and used in the CG technique. Additionally, we computed the streamwise effective wall friction coefficient at the bottom flat or rough wall as the ratio of the average force in the flow direction x and the average force normal on the wall (in y direction): $\mu_w = F_x/F_y$ (Artoni & Richard, 2015), which corresponds to the stress ratio τ_{xy}/τ_{yy} at the wall. The slip velocity was calculated as the average of all velocities for all particles in contact with the wall. The streamwise velocity fluctuations, which are related to the internal granular temperature of the flow, were also calculated as $T_x = \langle (V_x - \langle V_x \rangle)^2 \rangle$, where streamwise slip velocity fluctuations are calculated with respect to the average particle velocity (Artoni & Richard, 2015).

In order to show the effect of excess pore pressure on the granular bed strength, we simulate the failure of a static bed placed on an inclined slope that is lower than the angle of repose of the material ~19.5°. The angle of repose was obtained by piling up the granular material and measuring the slope of the surface. The excess pore pressure was generated by injecting air at the base of the domain at specified superficial velocity (volume flow rate divided by cross-sectional area). This allows us to modulate the excess pore pressure throughout the bed.
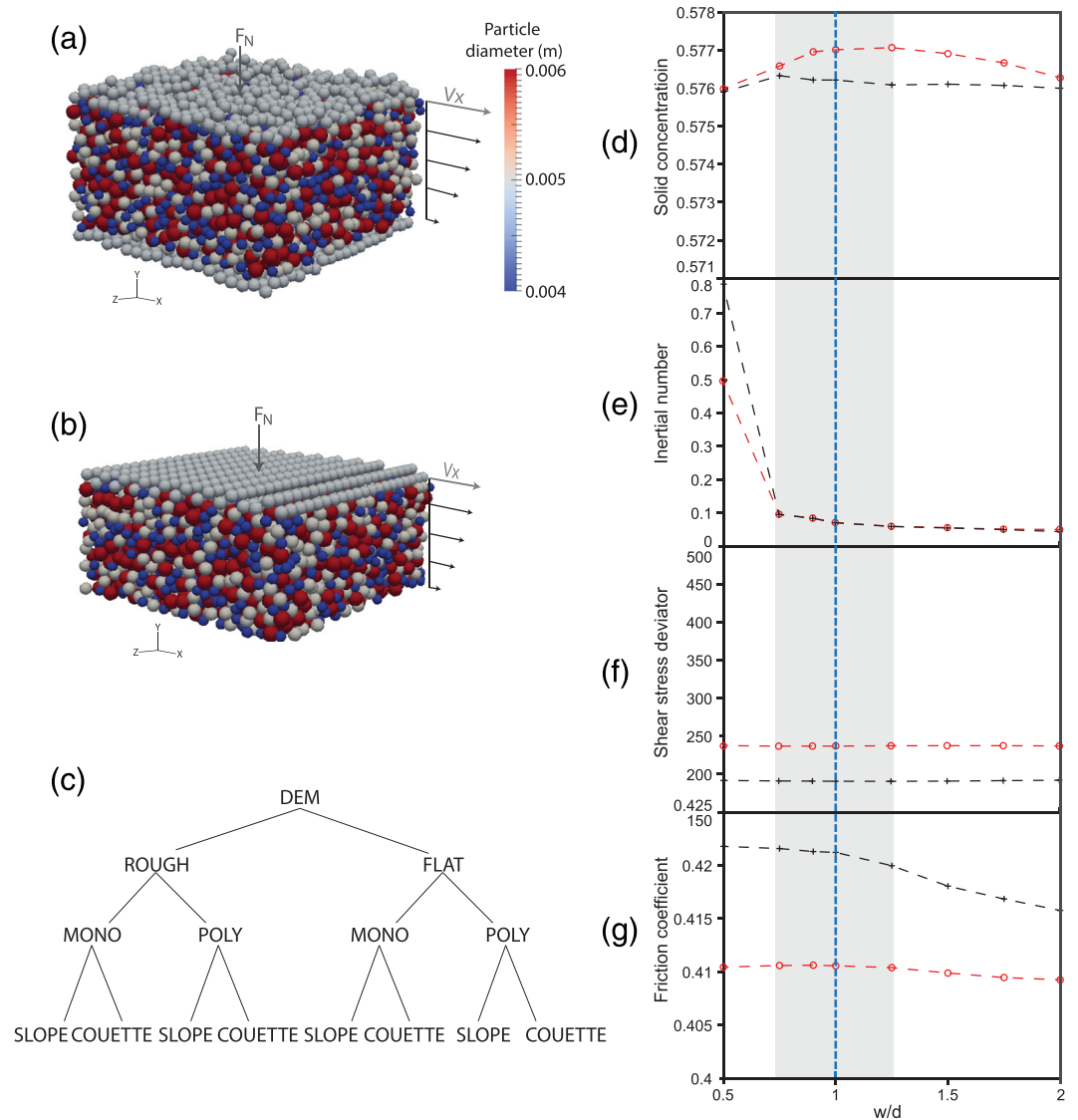
Figure 1. DEM Couette setup where a horizontal velocity (V_x) and average force (F_N) is applied from the top plate onto the bed that is placed across a rough substrate (a). (b) Similar to (a), with a flat friction basal boundary. (c) Simulation tree describing the various simulations undertaken in this study. Dependence of solid concentration (d), inertial number (e), shear stress (f), and friction coefficient (g) on w/d in the bed at 0.03 m (red data) and 0.05 m (black data) above the bed base. The blue line represents the $w/d = 1$ value chosen for the study. The grayed area shows the range of w/d values suggested by Weinhart et al. (2016).

The pore pressure is calculated as the differential fluid pressure between the absolute pressure at a given location and the ambient pressure. This pressure is that of the fluid and is different from that generated by particle interactions, which is called the solid pressure. To calculate the fractional pore pressure $P_g{}^*$ and solid pressure $P_s{}^*$, we calculate the hydrostatic pressure as

$$P_{hydrostatic} = g\int_{y0}^{y1}\rho dy, \tag{6}$$

where ρ is the mixture density. We thus defined $P_g{}^* = \dfrac{P_g}{P_{hydrostatic}}$ and $P_s{}^* = \dfrac{P_s}{P_{hydrostatic}}$, which allows us to track the degree of bed support due to the presence of excess pore pressure.

2.2. CG

CG techniques, also referred to the micro-macro transition (Weinhart et al., 2016), are applied to the particle data from DEM simulations to calculate (from discrete quantities) continuum fields such as density, velocities, and stresses, which are important for the analysis of the granular flow rheology. The development of the CG techniques and its use in granular mechanics is relatively recent and was first developed for monodisperse systems (Goldhirsch, 2010; Weinhart et al., 2013). CG has been successfully used to recover the rheology of various systems in 3-D and tested against experiments (Fullard et al., 2019). In the present study, the monodisperse CG method was adapted to describe monodisperse and polydisperse granular systems.

2.2.1. Polydisperse Equations

2.2.1.1. Coarse-Grained Momentum

As in statistical mechanics, one assumes the particle mass m_i is located at its center $\boldsymbol{r}_i(t)$ and define a microscopic (point) mass density at a point $\boldsymbol{r}$. From the convolution of the microscopic mass density using a CG function $W(\boldsymbol{r})$ (see Equation 14), we define the macroscopic momentum density $\boldsymbol{p^q}(\boldsymbol{r}, t)$ for each class q (from 1 to Q):

$$\boldsymbol{p^q}(\boldsymbol{r}, t) = \sum_{i \in q} m_i \boldsymbol{v}_i W(\boldsymbol{r} - \boldsymbol{r}_i(t)). \tag{7}$$

Vectors are shown in bold, and each operation is performed on the orthogonal vector components in 3-D. $\boldsymbol{v}_i$ is the velocity vector of particle i. A partial velocity field, $\boldsymbol{u^q}(\boldsymbol{r}, t)$ can be calculated as the ratio of the momentum density and the macroscopic mass density:

$$\boldsymbol{u^q}(\boldsymbol{r}, t) = \frac{\boldsymbol{p^q}(\boldsymbol{r}, t)}{\rho^q(\boldsymbol{r}, t)}. \tag{8}$$

The mixture bulk momentum density is defined as follows:

$$\boldsymbol{p}(\boldsymbol{r}, t) = \sum_{q=1}^{Q} \boldsymbol{p^q}(\boldsymbol{r}, t). \tag{9}$$

The partial bulk density of each particle class is given by CG:

$$\rho^q(r, t) = \sum_{i \in q} m_i W(\boldsymbol{r} - \boldsymbol{r}_i(t)). \tag{10}$$

Note that the bulk density of the mixture of particles is the sum of the partial ones:

$$\rho(r, t) = \sum_{q=1}^{Q} \rho^q(\boldsymbol{r}, t). \tag{11}$$

Each component of the mixture bulk velocity vector is given by

$$\boldsymbol{u} = \frac{\boldsymbol{p}(\boldsymbol{r}, t)}{\rho(\boldsymbol{r}, t)}. \tag{12}$$

2.2.1.2. Coarse-Grained Stress Tensor

Considering the momentum conservation equation, the partial stress tensor, $\sigma_{\alpha\gamma}^q$, is given as the sum of a kinetic, $\sigma_{\alpha\gamma}^{k, q}$, and contact contribution, $\sigma_{\alpha\gamma}^{c, q}$ such that

$$\sigma_{\alpha\gamma}^q = \sigma_{\alpha\gamma}^{k, q} + \sigma_{\alpha\gamma}^{c, q}. \tag{13}$$

The α, γ entry in the partial kinetic stress tensor is given by

$$\sigma_{\alpha\gamma}^{k, q} = \sum_{i \in q} m_i v_{i\alpha}^{'} v_{i\gamma}^{'} W(\boldsymbol{r} - \boldsymbol{r}_i(t)), \tag{14}$$

where $v_{i\alpha}^{'}$ is the α component of the fluctuation velocity of particle i.

$$v'_{i\alpha} = u_\alpha{}^q(\boldsymbol{r}, t) - v_{i\alpha}(t). \tag{15}$$

The mixture kinetic stress tensor is given by

$$\sigma^k(r, t) = \sum_{q=1}^{Q} \sigma^{k,q}(\boldsymbol{r}, t). \tag{16}$$

The calculation of the partial contact stress tensor differs slightly from the other partial fields. While the partial density, momentum, and kinetic stress tensors involve only particles from their own class q, the contact stress tensor involves the calculation of forces between particles in class q and particles from all classes, $v \in \overline{Q}$, where $\overline{Q}$ is the union of all particles classes, q. The α and γ entry in the partial contact stress tensor is given by

$$\sigma_{\alpha\gamma}^{c,q} = \sum_{i \in q} \sum_{j \in \overline{Q}} j \neq i f_{ij\alpha} \boldsymbol{a}_{ij\gamma} \int_0^1 W(\boldsymbol{r} - \boldsymbol{r}_i + s\boldsymbol{a}_{ij}) ds, \tag{17}$$

where $\boldsymbol{a}_{ij} = \boldsymbol{r}_i - \boldsymbol{c}_{ij}$ is as the branch vector between two particles, i and j, in contact and $\boldsymbol{c}_{ij}$ is the contact point. Note that for equally sized particles, the relationship above implies that the force between two particles f_{ij} is partitioned evenly. However, when particles are of different size, it is shown by Equation 9 that the contact stress is dominated by the larger particle.

The mixture contact stress tensor is given by

$$\sigma^c(\boldsymbol{r}, t) = \sum_{q=1}^{Q} \sigma^{c,q}(\boldsymbol{r}, t). \tag{18}$$

The mixture total stress tensor is simply the sum of the kinetic and contact stress tensors:

$$\sigma(\boldsymbol{r}, t) = \sigma^k(\boldsymbol{r}, t) + \sigma^c(\boldsymbol{r}, t). \tag{19}$$

The granular temperature inside the mixture is not the same as the granular temperature T_x calculated from the slip velocity (T_x, T_y, and T_z). T_g, can be defined from the trace of the mixture kinetic stress tensor and mixture density:

$$T_g = \frac{tr(\sigma^k)}{3\rho}. \tag{20}$$

The granular temperature is generally assumed isotropic (Zhang & Kamrin, 2017). Nevertheless, we will show that the granular temperature can be decomposed in its three components in order to illustrate a possible anisotropy (i.e., $T_{gx} = \frac{\sigma_{xx}{}^k}{\rho}$).

The average normal stress or solid pressure in the system is calculated as follows:

$$P_s = \frac{1}{3} tr(\sigma). \tag{21}$$

2.2.2. CG Function
In the present work, we choose the Gaussian CG function:

$$W(\boldsymbol{r}) = \begin{cases} V_w^{-1} exp \dfrac{-|\boldsymbol{r}|^2}{2w^2}, & for |\boldsymbol{r}| < c \\ \\ 0, & otherwise, \end{cases} \tag{22}$$

where the cut-off length is $c = 3w$, with w as CG width. Weinhart et al. (2016) suggest a value $0.75 \le w/d \le 1.25$, where d is mean particle diameter $d = \sum x_i d_i$ and x_i the normalized volume fraction of particle of diameter d_i, with $\sum x_i = 1$. We show that in this range, the flow properties measured from CG are scale independent and chose $w/d = 1$ (Figures 1d–1g).

V_w is chosen to ensure that the integral of the density is equal to the total mass:

$$V_w = 2\sqrt{2}w^3\pi^{3/2}erf\left(\frac{c\sqrt{2}}{2w}\right) - 4cw^2 \ \pi exp\left(\frac{-c^2}{2w^2}\right). \tag{23}$$

2.2.3. Calculation of Parameters to Measure the Rheology of Granular Mixtures

To further average our continuum fields, we spatially average the flows in the z direction (flow is moving in the x direction and gravity is in the xy dimensions). For a general field, G, this average is obtained the following way:

$$\acute{G} = \frac{1}{z_1 - z_0}\int_{z_0}^{z_1}Gdz, \tag{24}$$

where z_0 and z_1 denote the front and back of the domain in the z dimension. Therefore, we are left with thickness-averaged fields in the y and x directions. It was found that the shear component in the z direction was relatively small (plane strain condition), so intuitively, one would assume that the 3-D version of the stress tensor is best to use. However, comparing the friction coefficient with the angle of repose and steady state cases with and without pore pressure gave a better match to the tan (slope) (<4% error) when using the 2-D version of the stress tensor rather than the 3-D version (up to 13% error). The 2-D version of the stress tensor in combination with the pressure using all three contributions is always used in plane shear configuration (Chialvo & Sundaresan, 2013; Gallier et al., 2014; Ness & Sun, 2015; Weinhart et al., 2016; Zhang & Kamrin, 2017). Thus, we proceed with the 2-D version of the stress tensor:

$$\sigma^{2d} = \begin{pmatrix} \sigma_{xx}\sigma_{xy} \\ \sigma_{yx}\sigma_{yy} \end{pmatrix}. \tag{25}$$

The thickness-averaged mixture deviator stress tensor is given as follows:

$$\acute{\sigma}^{D, \, 2d}(r, \, t) = \acute{\sigma}^{2d}(r, \, t) - \frac{1}{2}tr(\acute{\sigma}^{2d}). \tag{26}$$

Dropping the $2d$ superscript and the magnitude of the tensor is defined as follows:

$$\left|\acute{\sigma}^{D}\right| = \sqrt{0.5\acute{\sigma}^{D}_{ij}\acute{\sigma}^{D}_{ij}}. \tag{27}$$

From this, we calculate the granular friction coefficient as the ratio of the shear stress and solid pressure:

$$\mu = \left|\acute{\sigma}^{D}\right|/\acute{p}_s. \tag{28}$$

To investigate granular flow rheology, one essential parameter to calculate is the domain-averaged inertial number:

$$I = \frac{\dot{\gamma}\acute{d}}{\sqrt{\frac{\acute{P}_s}{\rho_s}}}, \tag{29}$$

where ρ_s is the solid density, $\dot{\gamma}$ is the shear rate, and $\acute{d}$ is the mean particle diameter.

For polydisperse systems, the inertial number is calculated with the mean particle diameter $\acute{d}$ known as the D43 (Gu et al., 2016), which is the volume average mean diameter:

$$\acute{d} = D_{43} = n_q d_q, \tag{30}$$

where n_q is the mass fraction of the particle class q of diameter d_q.

The inertial number I is also a function of a shear rate $\dot{\gamma}$. To calculate the domain average shear rate, we first average the velocity fields in the z direction (depth direction). Then, we calculate the shear rate tensor in 2-D.

$$\dot{\gamma}_{ij} = \frac{\partial u_i}{\partial x_j} + \frac{\partial u_j}{\partial x_i}. \tag{31}$$

We calculate the shear rate deviator:

$$\dot{\gamma}_{ij}{}^d = \dot{\gamma}_{ij} - \dot{\gamma}_{ii}\delta_{ij}, \tag{32}$$

where δ_{ij} is the kronecker delta. We thus define the second invariant of the deviator as follows:

$$\left|\dot{\gamma}_{ij}{}^d\right| = \sqrt{\frac{1}{2}\dot{\gamma}_{ij}{}^d\dot{\gamma}_{ij}{}^d}. \tag{33}$$

An average is taken in the x direction (the direction of flow) to produce a vertical line of averaged shear rates:

$$\left|\dot{\gamma}_{ij}{}^d\right|_{verticalaverage} = \frac{1}{x_1 - x_0}\int_{x_0}^{x_1}\left|\dot{\gamma}_{ij}{}^d\right|dx. \tag{34}$$

And then average in the y direction

$$\dot{\gamma} = \left|\dot{\gamma}_{ij}{}^d\right|_{domainaverage} = \frac{1}{y_1 - y_0}\int_{y_0}^{y_1}\left|\dot{\gamma}_{ij}{}^d\right|_{verticalaverage}dy. \tag{35}$$

In further sections, we simplify the notations of the following terms: We use $\dot{\gamma} = \left|\dot{\gamma}_{ij}{}^d\right|_{domainaverage}$, P'_s as P_s and $\left|\sigma'^D\right|$ as σ.

3. Results

3.1. Rheology of Gas-Particle Granular Mixtures

The role of the dissipative timescale can be compared to the shearing timescale using the Stokes number defined by Boyer et al. (2011) as $St = \dot{\gamma}d^2\rho_p/\eta_f$. The Stokes number is $5 \times 10^0 < St < 7 \times 10^5$ for all simulations (in air and water) in the intermediate and inertial regimes. Calculating the Stokes number in the quasi-static regime is not meaningful for our application since this regime is dominated by particle contact, which generates a dense force chain network (Ness & Sun, 2015). Since all our simulations display particle volumetric concentration below the critical concentration Φ_{max}, shear thickening behavior is solely observed and the quasi-Newtonian or shear thinning behavior, which can only exist for $St < 1$, is not observed (Ness & Sun, 2015). This implies that while we simulate flows with pore pressure gradients where drag reduces the normal stress, the particle interactions are negligibly influenced (delayed) by viscous forces. In addition, the particle Reynolds (Table S1), which assesses the fluid inertial over viscous forces, exceeds 10 when the air- and water-particle beds are undergoing partial to full fluidization. Hence, the granular mixture is controlled by the single dimensionless parameter known as inertial number 29. The inertial number represents the ratio of time scale for rearrangement over deformation (GDR-MiDi, 2004). For the simulation in water, the shear rate is low enough to limit the role of viscous and lubrication forces so that the viscous number is up to an order of magnitude lower than the inertial number in the intermediate and inertial regimes. As a result, the shear stress and solid concentration in our simulations are a function of I only.

$$\tau = \mu(I)\, P \text{ and } \Phi = \Phi(I), \tag{36}$$

The functions $\mu(I)$ and $\Phi(I)$ measured in the discrete numerical simulations for the monodisperse (Figures 2a and 2b) and slightly polydisperse systems (Figures 2c and 2d) show the same trends. The solid concentration declines whereas the friction coefficient increases with increasing inertial number. The overlap of the data for a mean grain size diameter of 0.5 and 5 mm validates the unique control of the inertial number on the flow rheology. Based upon the polydisperse numerical rheology data, we fit the concentration data with the following law:
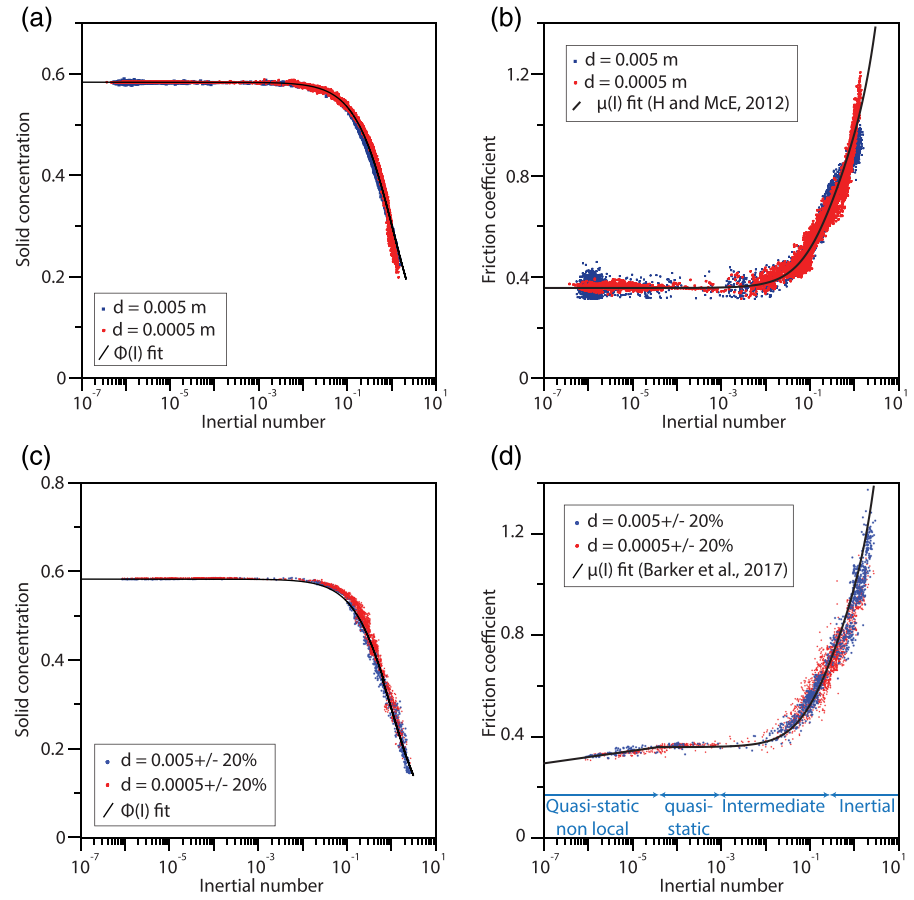
Figure 2. $\mu(I)$ and $\Phi(I)$ rheology of monodisperse and polydisperse granular flows simulated with discrete element modeling (DEM). Solid concentration (a) and friction coefficient (b) versus inertial number plot for the monodisperse mixture. Solid concentration (c) and friction coefficient (d) versus inertial number for the polydisperse mixture. The fit presented in (a) and (c) are from the Equation 37, and the fit in (b) is from Equation 38 and (d) is from Equations 38 and 39.

$$\Phi(I) = \frac{\Phi_{max}}{1 + aI} \tag{37}$$

(Amarsid et al., 2017) where a was found to be equal to 1 and $\Phi_{max} = 0.582$. This definition is similar to that describing granular flows immersed in a viscous fluid as introduced by Boyer et al. (2011), where I becomes $\sqrt{I_v}$ since viscous forces at the particle scale are dominant.

In the literature, granular flow regime boundaries have been loosely defined based upon the value of the inertial number. Three distinct regimes are as follows: the quasi-static, the intermediate, and the inertial regimes. We define four granular regimes from the slightly polydisperse cases based upon our simulations: quasi-static nonlocal (creep), quasi-static, intermediate, and inertial.

The quasi static regime is typically defined for $I < 10^{-3}$ since it defines roughly the threshold above which both solid fraction and the friction coefficient change abruptly. However, recent evidence indicates that an upper bound for I of the order 10^{-5} for the quasi-static regime may be appropriate because creep always persists (Houssais et al., 2015). Recently, creep has been detected at small values in laboratory experiments (Jerolmack & Daniels, 2019). In fact, while the friction coefficient appears to tend to a constant value equal to the tangent of the angle of repose of the granular mixture (~0.355), for $I < 4 \times 10^{-5}$, the friction coefficient decreases below the critical value of 0.355 in the simulations with polydisperse mixtures (Figure 2d). Similar creep behavior has been observed in granular mixtures immersed in viscous fluid (Houssais et al., 2016) and is characterized by intermittent and localized particle rearrangements that do not result in changes in

particle volumetric concentration. We name this behavior ***quasi-static nonlocal***, which bears similarities with amorphous solids such as glass. Importantly, particle rearrangement at $I < \sim 10^{-5}$ seem plausible in polydisperse systems but absent in purely monodisperse dispersions that can "crystallize" (Figure 2b). In addition, we define the ***quasi-static*** regime for $4 \times 10^{-5} < I < 10^{-3}$, where the particle volumetric concentration and friction coefficients are constant. To our knowledge, such crystallization solely exists in the numerical simulations since granular distributions in nature are never truly monodisperse.

For inertial numbers of 10^{-3} to 5×10^{-1}, the flows are in the ***intermediate*** regime, with a rheology following the $\mu(I)$ defined by Jop et al. (2006). In this regime, particles endure prolonged contacts. Finally, in the ***inertial*** regime, solid concentrations is low (<0.4–0.35). This has been defined as the inertial regime where binary collisions dominate the particle-particle interactions.

The decline of the friction coefficient below the tangent of the angle of repose in the quasi-static regime is in line with the findings of Barker et al. (2015), Barker et al. (2017), and Schaeffer et al. (2019) who showed that the constitutive equations of the $\mu(I)$-rheology are ill posed for low- and high-inertial numbers. The ill-posedness yields oscillations, instabilities, and sensitivity of the solution to the initial parameters (Gesenhues et al., 2019). The need to regularize the implementation of the $\mu(I)$ in continuum models led to the development of Equation 38, implying that as I tends to 0; the friction also tends to 0. Similarly, we fitted our DEM-CFD data with the same law proposed by Barker et al. (2017). The friction coefficient is fitted with a function describing the quasi-static, intermediate, and inertial regimes:

$$
\mu(I) = \left(\begin{array}{ll} \sqrt{\dfrac{\alpha}{ln\left(\dfrac{A_1}{I}\right)}} & I \leq I_1^N \\[4ex] \dfrac{\mu_{static}I_0 + \mu_d I + \mu_\infty I^2}{I_0 + I} & I > I_1^N \end{array} \right), \tag{38}
$$

$$
A_1 = I_1^N \exp\left(\dfrac{\alpha\left(I_0 + I_1^N\right)^2}{\left(\mu_{static}I_0 + \mu_d I_1^N + \mu_\infty \left(I_1^N\right)^2\right)^2} \right), \tag{39}
$$

where A_1, I_0, μ_∞, μ_d, and α are constants. I_1^N is the lower end of I where Equation 31 is well posed. The form of the friction coefficient at high-inertial number is based on the experimental work of Holyoake and McElwaine (2012). We find $A_1 = 140$, $\mu_{static} = 0.355$, $\mu_d = 1$, $\mu_\infty = 0.2$, $\alpha = 1$, and $I_0 = 0.3$.

Figure 2d shows that $I_1^N = 4 \times 10^{-5}$ fits well the decline of friction below the tangent of the angle of repose. To our knowledge, this is the first numerical study confirming that athermal creep in granular material immersed in air without an external flowing layer can lead to a friction coefficient becoming lower than the tangent of the angle of repose.

Now that we have described the flow rheology and the relationship between the internal friction coefficient with the scaled shear rate (inertial number), we describe the flow-substrate interactions and scaling.

3.2. Slip Velocity on Flat Friction Surfaces

Many small to large-scale experiments have been designed to investigate mass flows and simulate granular mixtures moving across a flat frictional surface at their base (and often on their side walls). The term flat frictional implies that the roughness is orders of magnitude smaller than the particle diameter and that the particle-wall friction coefficient μ_{pw} is >0. This friction coefficient comprises the effect of particles rolling and bouncing on the flat interface. For instance, glass beads typically roll on a 11° slope, whereas their μ_{pw} is ~tangent (21.5°) (O. Roche, personal communication, September 11, 2018). Quantifying the relationship between basal slip and basal wall friction is necessary to better understand the experiments and to define boundary conditions, which are crucial parameters feeding numerical models.

Here we assess the interactions between granular flows and solid interface by measuring the forces at the bottom surface and the velocity of particles impacting it. We restrict the analysis to the streamwise component of the force and slip velocity since their magnitude are orders of magnitude larger than their cross stream components. In a single DEM simulation, we incline over time a monodisperse and slightly
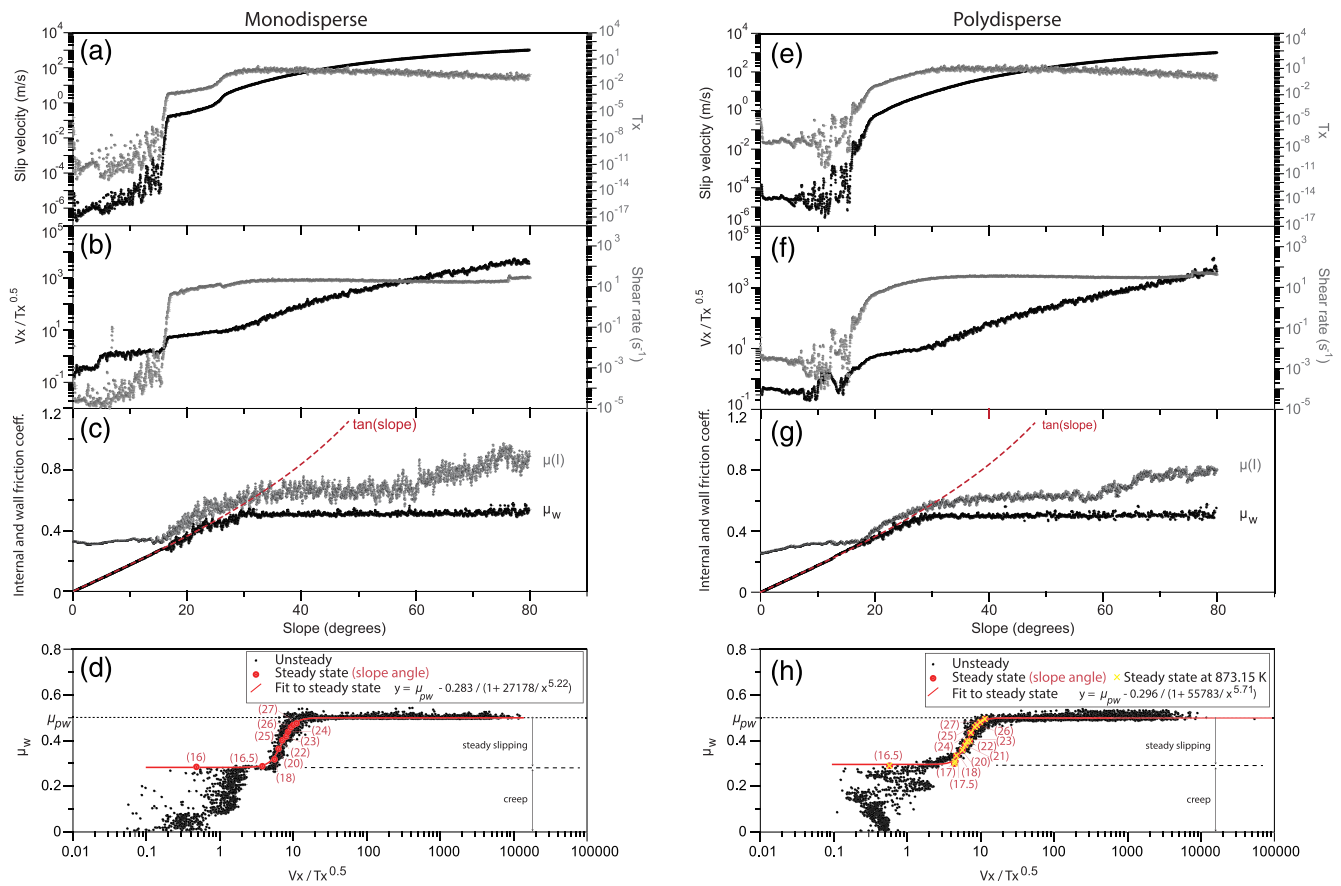
Figure 3. Scaling of the wall friction for monodisperse and polydisperse beds moving across a flat frictional substrate. The slip velocity and slip fluctuations (a), nondimensional slip ($V_x/\sqrt{T_x}$) and shear rate (b), and internal $\mu(I)$ and wall friction (μ_w) coefficients (c) for the monodisperse mixture of 5 mm spherical particles are plotted against the slope of the flat frictional substrate. For the polydisperse case, made of 4.5 to 5.5 mm spherical grains, the slip velocity (e), nondimensional slip ($V_x/\sqrt{T_x}$) (f), and internal $\mu(I)$ and wall friction (μ_w) coefficients (g) are plotted against the slope of the flat frictional substrate. Note that μ_{pw} is the particle wall friction coefficient set in the DEM simulation as =0.5. In (c) and (g), the red dash line represents the tangent of the slope angle. Wall friction coefficient scaled versus the nondimensional slip parameter for the monodisperse (g) and polydisperse (h) simulations. The ref line is the fit to the steady state simulations (red dots), while the black dots are from the unsteady simulation. In (h), the steady state simulations were replicated at 873.15 K (yellow cross) and overlap with the ambient temperature (red dots).

polydisperse particulate mixture from a horizontal slope up to 80°. The inclination rate is 0.2°/s, which is a half order of magnitude lower than the relaxation time of the granular bed found to be 1.1°/s (Figure S1), which ensures that our result from the inclined simulations are equivalent to steady state situations. We present measurements of the rheology of the basal portion of the flow of a thickness equal to 3 particle diameters and the slip and force measurements at the flat bottom surface.

On a slope of 0.2–17.5°, the flow is slipping in a creep regime as depicted by the small slip velocity (10^{-7} to 10^{-4} m/s), accompanied by spatial fluctuations of the slip velocity T_x (Figures 3a and 3e). Creep consists of stick-slip events where slip changes by an order of magnitude in <1 s. Simultaneously, the shear rate in the flow base mimics the slip velocity and its fluctuations (Figures 3b and 3f). The nondimensional slip velocity defined as $V_x/\sqrt{T_x}$ shows that spatial velocity fluctuations are correlated with slip velocity. For a slope exceeding 17.5° that corresponds to the tangent of the $\mu_{slip-threshold}$, the flow rapidly changes from creeping to sliding, as depicted by rapid change of shear rate, slip velocity, and slip velocity fluctuations. The velocity fluctuations and shear rate increase up to a slope of 30°, the nondimensional slip increases with slope. Interestingly, the trends of all parameters are similar between the monodisperse and polydisperse cases.

The basal friction coefficient matches the tangent of the slope up to a slope inclination 24° for the monodisperse case (Figure 3c) and 21° for the polydisperse simulation (Figure 3g). Above this threshold, the basal

friction coefficient tends to a constant value of 0.5, which matches the value of μ_{pw} imposed. At all times, the internal friction coefficient exceeds the wall friction in the monodisperse scenario, whereas the basal and internal friction coefficients are equal for a slope of 15°.

In order to study the effective wall friction in detail, we discuss its scaling with flow parameters. By similarity with the kinetic theory of gases on flat frictional walls (Jenkins, 1992; Johnson & Jackson, 1987), the slip velocity can be scaled with its fluctuations. As shown by Artoni & Richard (2015), the slip velocity fluctuations scale with the shear rate, which suggests that $\sqrt{T_x}$ can be used to test the scaling of the slip velocity. Figures 3d and 3h show the relationship between the wall friction μ_w and $V_x/\sqrt{T_x}$ for a single simulation where the slope is inclined slowly over time and for steady state simulations with a constant slope inclination spanning 16°/16.5° to 27° (monodisperse/polydisperse). Beyond this range, a no slipping, steady state can be reached. Based on both monodisperse and polydisperse simulations, we define two regimes: (i) the creep and (ii) the steady sliding. In the creep regime, the correlation between μ_w and nondimensional slip $V_x/\sqrt{T_x}$ is not clear, particularly for the polydisperse case. This regime corresponds to slopes below the formation on continuous slipping and characterizes the slow creeping and stick-slip events occurring at low slope angle. In the steady slipping regime, a clear correlation exists between the wall friction and the slip velocity. The wall friction takes the functional form:

$$\mu_w = \frac{\mu_{pw} - a}{1 + b\left(V_x/\sqrt{T_x}\right)^c}, \tag{40}$$

where a is the tangent of the angle above which slips initiate and b and c are constants. Equation 40 bears similarities to the definition of Artoni and Richard (2015) for vertical wall friction and with the boundary conditions of kinetic theory of granular flows (Jenkins, 1992; Johnson & Jackson, 1987; Richman, 1988). Additionally, the results provide a rapid way of estimating the maximum μ_w expected for a mixture on a given flat frictional boundary. By determining the maximum slope where the slip velocity reaches steady state (here 27°), one can estimate the plateau of μ_w (~tan 27°) or alternatively could be used as a boundary term of granular temperature.

While geophysical flow generally propagates on rough substrates, our analysis is useful to understand the scaling of the wall friction on flat surfaces, which occur in experimental setups (Roche et al., 2016) and on manmade structures in nature. For instance, when debris flows move atop force plates placed in the substrate to measure impact forces (Kean et al., 2015). Similar basal measurements would be essential to understand the mechanics of pyroclastic density currents. These currents are very hazardous, in part, because of their high temperatures. To test whether temperature is a controlling factor of the wall friction, we replicated steady state simulations with a temperature of 873.15 K. The increase of gas temperature yields a decrease of the gas density (~300% decrease) and increase in fluid viscosity (~100% increase) with respect to ambient fluid temperature. However, the data overlaps with the ambient temperature data. This suggests a negligible effect of temperature on the scaling of the wall friction.

3.3. Slip Velocity of Granular Flows on Rough Substrate

We extend our analysis to rough walls since granular flows in natural settings always propagate on a rough substrate (Booth et al., 2014; Prancevic & Lamb, 2015), regardless of whether particles fall individually or as coherent flows. Previous numerical work has focused on steady, monodisperse, inelastic, frictionless spheres between parallel plates (Berzi & Vescovi, 2017), with a roughness that was made of a lattice of glued spheres.

Here we first present results from a simulation with a mean roughness ψ of $6\pi/30$. Similar to the simulations on smooth frictional substrates, the simulation involved the slow destabilization of a quasi-static bed on an inclined slope. Because of the low number of particles in contact with the substrates on rapid flows on high slope, we restricted the analysis to slopes <66°. Figure 4 presents the time series data for a simulation involving a mixture of 400–600 μm spherical particles. On slopes ≤21°, the bed is creeping with slip velocity of 10^{-6} to 10^{-3} m.s^{-1} and shear rates of 10^{-4} to 10^{-1} s^{-1} and a nearly constant scaled slip velocity defined as $V_x/\sqrt{T_x}$. Simultaneously, the wall friction coefficient μ_w increases with slope and equals the tangent of the slope. The ratio of shear stress to normal stress calculated as the $\mu(I)$ shows that it exceeds the slope by ~10% and equals the μ_w at the slope where the flow transitioned into failure. At slopes of 21° to 40°, μ_w declines whereas $\mu(I)$ increases, while the $V_x/\sqrt{T_x}$ increases across 2 orders of magnitude. On slopes >40°,
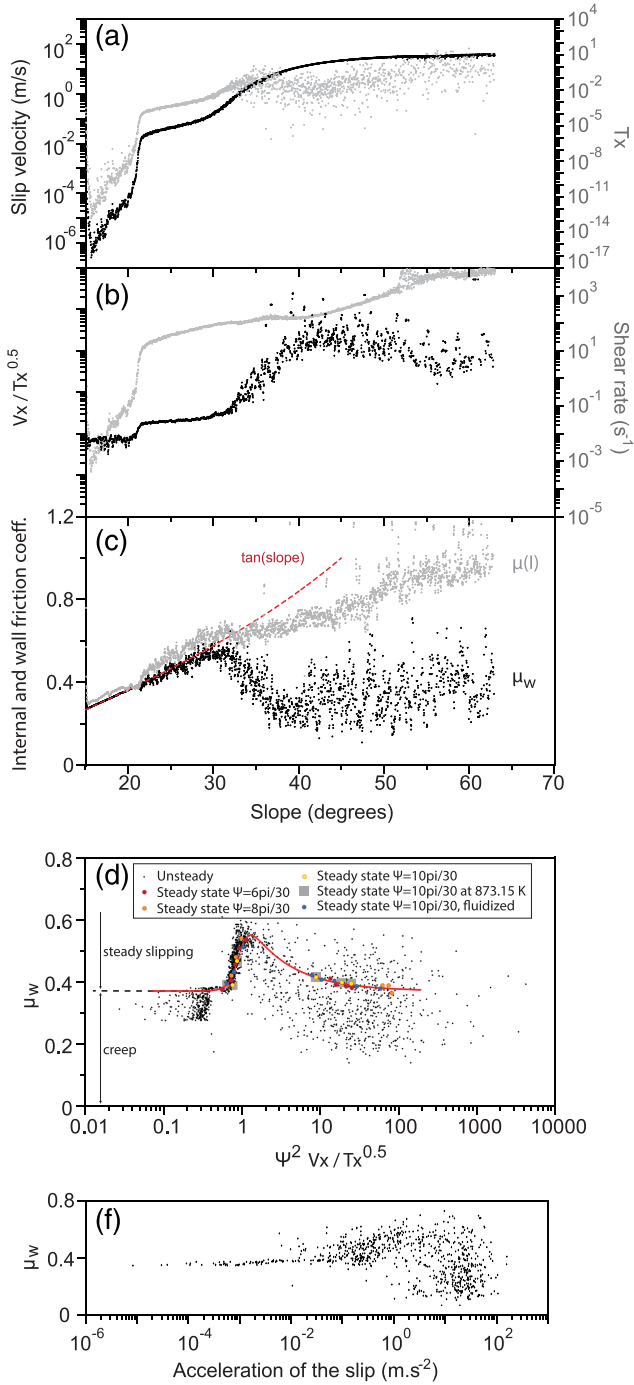
Figure 4. Scaling of the slip velocity for polydisperse mixtures on rough substrate. Slip velocity and slip fluctuations (a), shear rate and nondimensional slip ($V_x/\sqrt{T_x}$) (b), and internal $\mu(I)$ and wall friction (μ_w) coefficients (c) against the slope angle. (d) Wall friction versus nondimensional slip defined as the product $\psi^2 V_x/\sqrt{T_x}$. ψ describes the roughness (see the section 2). The red line is described by Equation 33 and fitted the steady state data. (f) Wall friction versus acceleration based upon the slip velocity.

μ_w increases slowly from the plateau ~0.3 to ~0.4. The apparent relationship between slip velocity and wall friction coefficient is depicted in Figure 4d. Similar to flows on a flat frictional surface (Figures 3d and 3h), the creep regime and steady slipping regimes are separated by a threshold (slope ~20° μ_w~0.37) above which steady state simulations can be achieved. This threshold corresponds to a sharp increase in $V_x/\sqrt{T_x}$. Above $V_x/\sqrt{T_x} = 1.9$, μ_w reaches values of 0.55–0.58, before declining rapidly to reach a plateau around 0.3–0.35 (with large scatter between ~0.15 and 0.55) for $V_x/\sqrt{T_x}$ >10. Steady state simulations on slopes of 24°, 26°, and 28° fall within the data scatter and give values of μ_w~0.35–0.4. This behavior is drastically different from that of flows on flat frictional surfaces and has only been reported once in the literature by Berzi and Vescovi (2017) for frictionless monodisperse mixtures.

We introduce the prediction of the wall friction coefficient as a function of the $V_x/\sqrt{T_x}$ and roughness parameter ψ:

$$\mu_w = \mu_{slip-thresold} + \left[\psi^2 V_x/\sqrt{T_x}\right]^e \left[a + b\left[\psi^2 V_x/\sqrt{T_x}\right]^d\right]^{-c}, \quad (41)$$

where $a = 3$, $b = 4$, $c = -1$, $d = 6.8$, $e = 6$, and $\mu_{slip-thresold}$ equals 0.37, which is similar to the tangent of the angle of repose of the material in the simulation. Equation 41 describes well the wall friction of steady state simulations for the range of roughnesses investigated (ψ=6–10π/30) (Figure 4d). The description above suggests that the basal friction coefficient is lowest when the flow is static, but for short durations, it fluctuates at high nondimensional slip and can reach values that are half that of the quasi-static wall friction coefficient.

Interestingly, the difference between flows in steady and unsteady states appears to be at high nondimensional slip, since μ_w tends to 0.35–0.4 for steady state whereas unsteady flows seem to show μ_w tending to 0.3–0.35. This appears to be linked to the temporal derivative of the slip velocity or acceleration ($\partial V_x/\partial t$). For an acceleration >1 m.s^{-2}, the μ_w decreases (Figure 4e). This surprising behavior is systematically observed when the flow accelerates, including steady state simulations (on constant slope). In simulations, acceleration exceeding 1 m.s^{-2} is short lived (<10s) and is unlikely to be occurring over longer timescales in natural settings, in part because the slope is often declining with runout distance from source.

Similar to the simulations on flat frictional walls, the temperature data overlaps with the ambient temperature data, suggesting that our findings are independent of the temperature within the range investigated (293.15–873.15 K) (Figure 4d). Most interestingly, we simulated partially fluidized steady state cases by injecting air at the base and sustaining an excess pressure in the bed. The wall friction data overlaps well with the data without pressure gradient, which suggests the presence of excess pore pressure does not modify the scaling of the friction coefficient. If excess pore pressure does not affect the scaling of the wall friction, how does pore pressure affect the rheology of the bed and how can we account for this in flow models?

3.4. The Role of Excess Pore Pressure: Granular Flows Immersed in Air and Water

We illustrate the role of excess pore pressure on the flow-substrate interactions by simulating the failure of a static bed. This examines the
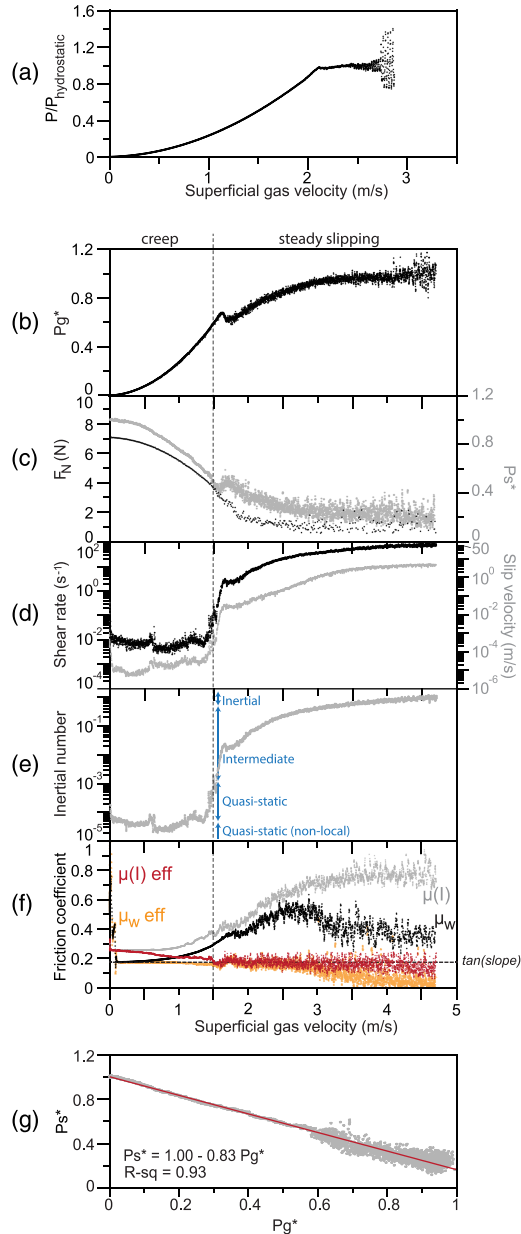
Figure 5. Evolution of the pore fluid pressure and wall and internal friction coefficients of the granular bed during failure on an inclined slope. (a) Scale-pore pressure at the flow base versus superficial gas velocity for the mixture on a horizontal slope. Full fluidization occurs at a superficial velocity of 2.15 m.s^{-1}. (b) Scaled pore pressure at the flow base versus superficial gas velocity. Note that shear prevents bubbling to occur. Full fluidization is reached at superficial velocity ~3.5 m.s^{-1}. The horizontal black dash line represents the tangent of the slope (=0.176). (c) Spatially averaged normal force exerted by the bed onto the rough substrate and scaled solid pressure $P_s^* = \frac{P_s}{P_s(start)}$. (d) Shear rate and slip velocity versus superficial gas velocity. (e) Inertial number. The quasi-static, quasi-static (nonlocal), and intermediate and inertial regimes defined from Figure 2 are shown. (f) Scaled pore pressure P_g^* versus scaled solid pressure P_s^*. The red dash line is the linear fit to the data. Data include superficial velocity <4 m/s, thus excluding the bubbling stage. (g) Visualization of the 3-D bed on the 10° incline slope.

transition from solid-like to fluid-like behavior induced solely by increasing the pore-fluid pressure progressively. When placed on a horizontal slope, the polydisperse bed composed of a mixture of spheres of 4 to 6 mm in diameter becomes fully fluidized at superficial gas velocity of 2.1 m.s^{-1} (Figure 5a). This bed is placed on a 10° incline slope and the superficial gas velocity is set to be 0 m.s^{-1}. Since the slope is 8.5° below the angle of repose, the flow is quasi-static (in creep regime). When increasing the superficial gas velocity from 0 to 1.25 m.s^{-1}, the nondimensional pore pressure ($P_g^* = \frac{P_g}{P_g hydrostatic}$) increases from 0% to 45% (Figure 5b). Meanwhile, the normal force (F_N) applied on the substrate decreases and mimics well the decrease of the internal solid pressure (Figure 5c). The slip velocity increases slowly by 1 order of magnitude whereas the shear rate remains relatively constant. Simultaneously, the wall (μ_w) and internal friction coefficients increase. When the superficial gas velocity reaches 1.48 m.s^{-1}, all bed properties rapidly change as the bed fails and transitions rapidly from creeping to slipping.

The transition into slipping is controlled by the ability of the bed to shear, which, in turn, depends on the effective friction coefficient that we define as the product:

$$\mu(I)_{eff} = \mu(I)P_s^*, \qquad (42)$$

with the scaled solid pressure P_s^*. For a superficial velocity of 1.48 m.s^{-1}, $\mu(I)_{eff} < tan$(slope), which yields the onset of the bed avalanching. Similar to the internal effective friction coefficient, we define an effective wall friction coefficient:

$$\mu_{w_{eff}} = \mu_w P_s^*, \qquad (43)$$

Note that measurements of basal forces from experiments with partially to fully fluidized beds would provide $\mu_{w_{eff}}$ since the normal force measured on the force plate would be that applied by particles and by the pore fluid pressure. Measurements of basal pore pressure are required to correct the normal force and estimate the true wall friction coefficient μ_w (assuming that the shear force applied on the force plate by air is negligible with respect to that applied by particles).

Interestingly, the transition between the creep and steady slippings (1.25–1.48 m.s^{-1}) coincides with a $\mu_{w_{eff}}$<tan (slope).

Excluding the phase where the bed is bubbling while sheared for superficial velocities exceeding ~4 m.s^{-1}, the relationship between the pore pressure and solid pressure scales linearly with a slope $\delta = -0.83$ (Figure 5g). Similar to our DEM simulations in air, there has been much evidence in water-saturated particle flows (debris flows) that contact stresses generate the largest contribution to the shear (Iverson & George, 2014).

In order to demonstrate the general applicability of our findings from gas-to water-particle flows, we simulated a static bed immersed in water and increased pore fluid pressure. This setting describes the behavior of a granular bed immersed in water, for example, (i) a bed that fails and generates submarine avalanche or (ii) the portion of a water-saturated mixture away from the free surface, which sits on a flank and destabilizes to form a debris flow.
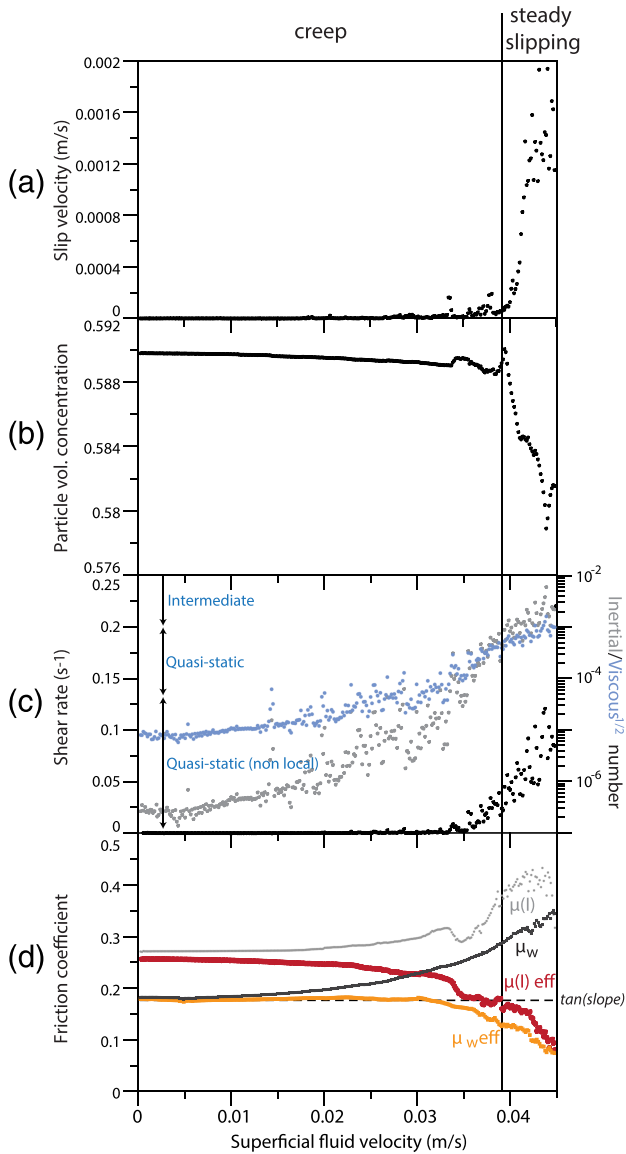
Figure 6. Destabilization of a granular bed immersed in water on an incline of 10°. Slip velocity (a), particle volumetric concentration (b), inertial number (*I*), and viscous$^{1/2}$ number $\sqrt{I_v}$ (c) versus superficial fluid velocity. The quasi-static, quasi-static (nonlocal), and intermediate and inertial regimes defined from Figure 2 are shown in Figure 2c. Note that a shift in the slopes occurs when the flow regime transitions from quasi-static to intermediate at an inertial number ~10^{-3}. (d) Friction coefficients ($\mu(I)$, $\mu(I)eff$, and μ_w, μ_weff) are plotted against the superficial fluid velocity. The horizontal dashed line indicates the tangent of the slope. Failure of the bed (steady slipping) occurs when $\mu(I)eff$ becomes lower than the tangent of the slope.

In a more viscous fluid, lubrication forces may play a role in controlling the particles' motion. Thus, we added a description of the normal and tangential lubrication forces to the MFIX-DEM code following the work of Carrara et al. (2019) and Marzougui et al. (2015). We show that similar to flows immersed in air, excess pore fluid pressure induces the failure of the bed immersed in water when the basal friction coefficient $\mu_{w_{eff}}$ and internal friction coefficient $\mu(I)_{eff}$ become lower than the tangent of the slope (Figures 6a–6d). The viscous number (Boyer et al., 2011) was calculated as $I_v = \dot\gamma \rho_s \eta_f / P_s$ and used to compare the role of the viscous over the inertial stress by plotting $\sqrt{I_v}$ against I (Amarsid et al., 2017). Since $\sqrt{I_v}$ is smaller than I (Figure 6c) in the intermediate regime and prior to the bed destabilization, inertial stresses dominate the motion of particles during failure and formation of the granular avalanche. Importantly, since the water-particle bed is controlled by the inertial number I, our results do not cover the range of muddy debris flows that sit in the viscous regime and are controlled by the viscous number (Iverson & George, 2014; Lube et al., 2020). While we used the notation $\mu(I)$ for the internal friction coefficient in this section, for completeness, the internal friction could be noted $\mu(I_m)$, where the visco-inertial number $I_m = I\sqrt{\left(1 + \frac{\alpha_v}{St}\right)}$, with α_v as a constant (Amarsid et al., 2017). However, the meaningful use of the Stokes number (St) is restricted to the intermediate and inertial regimes where $I_m > 10^{-3}$ (see section 2). Since our simulations span the quasistatic to intermediate regimes ($10^{-6} < I_m < 10^{-2}$), we decided to use the notation $\mu(I)$ instead of $\mu(I_m)$.

The bed appears to start slipping and is transitioning from quasi-static nonlocal to the quasi-static regime when $\mu_{w_{eff}} < \tan$ (slope) (Figure 6a). When $\mu(I)_{eff} < \tan$ (slope), the bed transitions to the quasi-static to the intermediate regime wherein dilation take place (Figure 6b) and can be properly described as destabilized/failing (Figures 6c and 6d). These findings confirm the validity of Equations 36 and 37, which hold to describe both failure and flowing behavior of the bed regardless of the nature of the fluid (air or water).

4. Discussion

Simulations reveal that polydisperse systems are prone to develop mechanical noise that yields nonzero granular temperature and subsequent athermal creep in concentrated granular systems. The latter process remains a frontier in soft-matter physics (Houssais et al., 2016; Jerolmack & Daniels, 2019) and describes a transient relaxation process that decays with time. In a system devoid of mechanical noise, creep should vanish logarithmically with time. However, in granular media, particles rearrange and introduce mechanical noise. In nature, mechanical noise is present at many scales, whether introduced by earthquakes, ground inflations, capillary forces, or pore fluid pressure. The phenomenological picture of such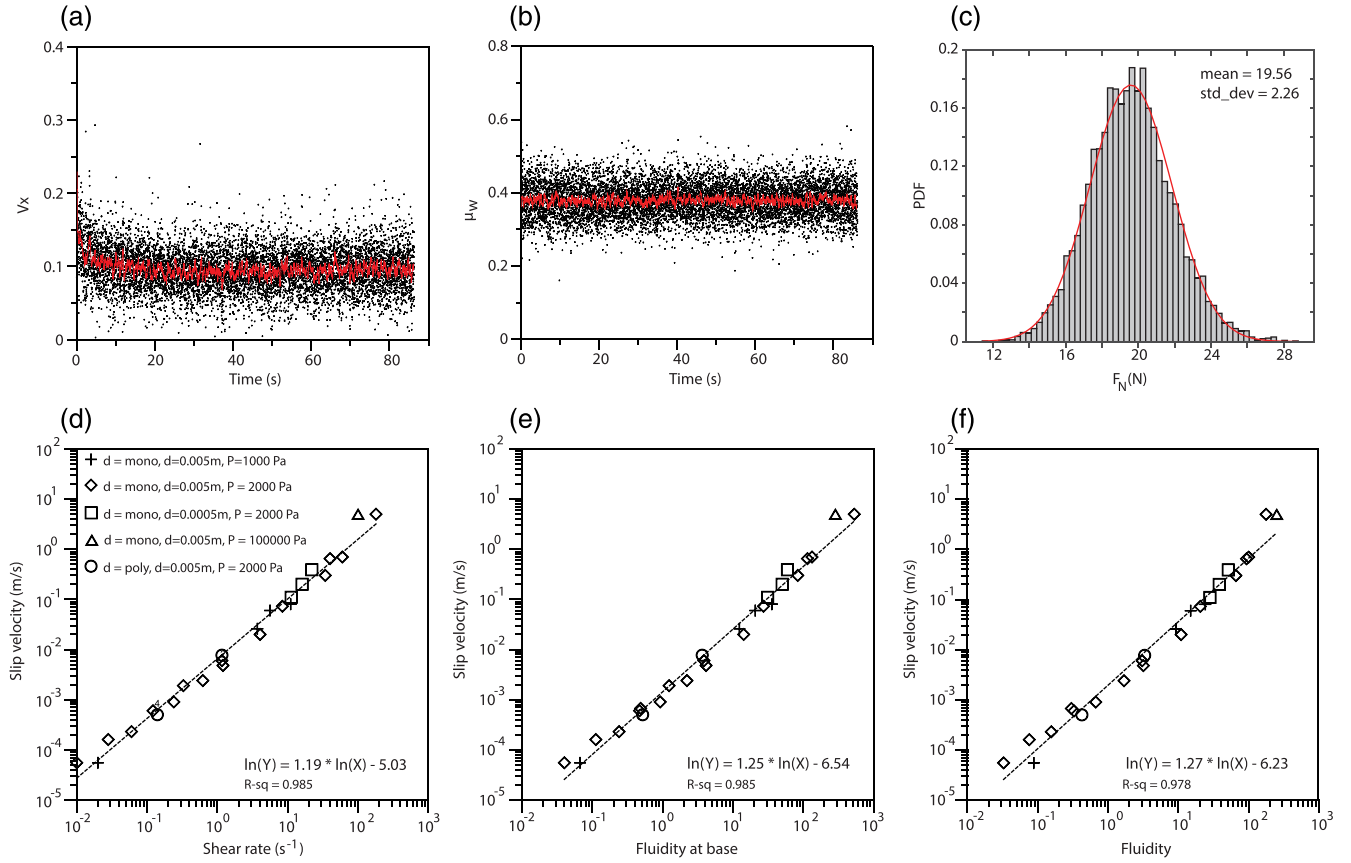 creep is that of glassy mechanics, which surprisingly implies that flows are never truly static. This field requires further attention from numerical approaches, where for instance continuum models that incorporate transport equations for granular temperature (i.e., MFIX) are best suited to describe the granular flow dynamics down to the athermal creep regime.

By studying internal shear to normal stress ratios at the wall (wall friction coefficient) and in the basal portion (internal friction coefficient) in quasi-static to inertial granular flows, we define three distinct behaviors: (i) waning slip velocity, (ii) steady slip velocity, and (iii) waxing slip velocity. Waning of the slip velocity is

Figure 7. Fluctuations in steady state simulations on a 20° incline and $\psi = 6\pi/30$ and scaling of the slip velocity boundary condition. Slip velocity (a) and wall friction coefficient versus time (b) at 100 Hz. The red line is the time average with a widow of 0.1 s. (c) Distribution of the mean normal force (F_N) measured at the basal wall at each time step fitted with a normal distribution (red line). Scaling of the slip velocity against shear rate (d), fluidity at base (e), and fluidity (f). Each data point represents one simulation.

expected if flows are given momentum and propagate on slopes that are lower than the arc tangent of $\mu_{slip-thresold}$. Flows propagating between the arc tangent of $\mu_{slip-thresold}$ and $\mu_{saturation}$ can reach steady state slip, whereas on slopes higher than the arc tangent of $\mu_{saturation}$ the slip velocity increases indefinitely.

Using a Couette setup, where a set force and velocity is applied by the plate onto a bed (Figure 1a), we show that all parameters reach steady state (slip velocity [Figure 7a] and wall friction coefficient [Figure 7b]). Subsequently, the time-variant normal force applied by the bed onto the rough substrate follows a normal distribution (Figure 7c). Such simulations allow a comparison of slip velocity for a given roughness ψ of $6\pi/30$ as a function of the strain rate deviator (also known as shear rate $\dot{\gamma}$), the fluidity at the base $g_{wall} = \mu_w/\dot{\gamma}$ and the fluidity $g_{flow} = \mu(I)/\dot{\gamma}$. For this comparison, we consider a set of 30 steady state Couette simulations where the confining force (F_N), the particle diameter and size distribution is varied. The slip velocity scales with $\dot{\gamma}$ (Figure 7d), g_{wall} (Figure 7e), and g_{flow} (Figure 7f) for a range spanning six orders of magnitude (10^{-3} to 10^3). Since the slip velocity and shear rate are not linearly correlated, this is not strictly speaking equivalent to a Navier slip but a nonlinear Navier slip where the slip length is given as $\exp(-4.199)$ (Figure 7d).

Here we report an additional observation related to the granular temperature, which is often assumed isotropic in continuum models (e.g., Kinetic theory; Syamlal et al., 2016). In Figure 8, we show that both granular temperatures in the bed and at rough substrate-flow interface are a function of the inertial number and are anisotropic for inertial number > $\sim 10^{-2}$. The streamwise component (X) is much larger (up to 7 times) than Y and Z components which are both equal to one another. The role of such anisotropy and scaling of the granular temperature with inertial number are beyond the scope of the paper, but it may be worth investigating in the future.
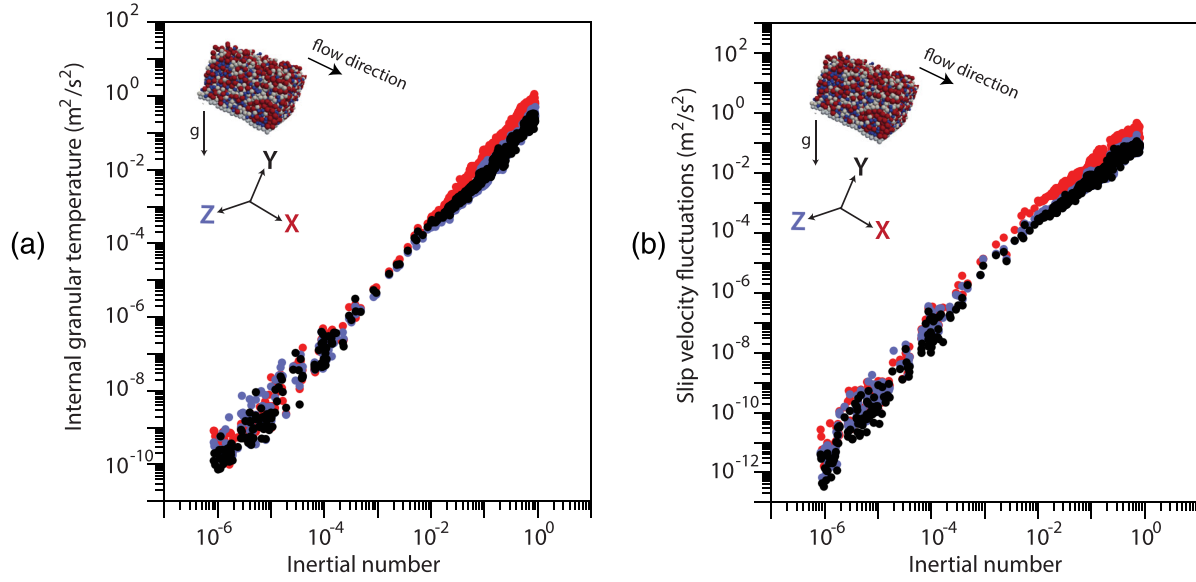
Figure 8. The 3-D components of the granular temperature (a) and slip velocity fluctuations (b). The X, Y, and Z components are shown in red, black, and blue, respectively. Note that Z and Y components are overlapping across the entire range of I investigated.

The simplicity of measuring wall friction, slip velocities, and their fluctuations in discrete element models contrasts with the large challenges faced in obtaining similar data from natural geophysical flows. However, such measurements would be key to understand the substrate erosion of debris flows (Kean et al., 2015) or pyroclastic density currents. In the absence of measurements in natural settings, the implementation of force sensors measuring wall normal and tangential components in large-scale experiments has helped to describe the evolution of shear stress with excess pore-fluid pressure for a sheared bed (Iverson, Logan, et al., 2010). Decades of research have shown that the presence of excess pore-fluid pressure is key to alleviate frictional stresses in debris flows (i.e., Iverson et al., 1997; Iverson, Reid, et al., 2010), pyroclastic density currents (i.e., Lube et al., 2019; Roche et al., 2016), and submarine avalanches (Urlaub et al., 2015) and explain their long runout and ability to propagate on shallow slopes. Here we aim to show how an excess pore fluid pressure modifies simultaneously the internal rheology of a granular flow and its interactions with a substrate. The pore pressure feedback (Iverson, 2005), which dictates how changes of particle volumetric fraction and pore pressure evolve concurrently, is a highly dynamic process.

Embedding the effect of pore pressure in a constitutive equation has been widely used in the debris flow community following the work of Iverson et al. (1997) and Iverson, Reid, et al. (2010). Similar to our DEM simulations in air, there have been much evidence in water-saturated particle flows (debris flows) that contact stresses generate the largest contribution to the shear (Iverson & George, 2014). Based upon our air- and water-particle simulations, we define a Coulomb rule that is rate dependent, as manifested by the $\mu(I)$, and defines a proportionality between shear stresses and normal stresses on planes of shearing. The basal and internal shear stresses for the solid is defined as follows:

$$\tau_{base} = \mu_w P_s = \mu_w(\sigma - \delta P_g). \tag{44}$$

μ_w is the wall friction that is a function of $\psi^2 V_x / \sqrt{T_x}$.

$$\tau_{internal} = \mu(I) P_s = \mu(I)(\sigma - \delta P_g). \tag{45}$$

σ is the hydrostatic pressure defined as $\rho g h_{normal}$, P_g is the pore fluid pressure, and δ is the slope correlating the solid to pore fluid pressure. The inertial number I can be substituted by the visco-inertial number I_m in Equation 45, if the viscous stress becomes large with respect to inertial stress.

These results have fundamental implications for our ability to describe and predict the behavior of polydisperse and fine-grained flows where low Sauter mean diameter (Breard et al., 2019) and low permeability can promote the development and sustainment of pore fluid pressure, as measured experimentally in water-rich debris flows (Iverson, Reid, et al., 2010), pyroclastic density currents (Lube et al., 2019), and submarine avalanches (Masson et al., 2006).

While we showed that air temperature does not affect the scaling of the wall friction, the higher the air temperature the longer the diffusion timescale of the excess pore pressure because of the increase of the fluid viscosity (Druitt et al., 2007), which ultimately affects the effective internal and basal shear stresses. Additionally, our wall friction scaling is independent of the particle diameter and flow thickness. A change in any of these flow properties would be reflected in the granular temperature and suggests that our scaling would hold. Most importantly, as all natural currents can be made of wide grain-sized distributions, there is a need to study the interplay of polydispersity on the permeability and granular stresses. This could be achieved through particle-resolved direct numerical simulations (PR-DNSs) that would enable the measure of granular temperature. Such measurements are much needed to scale the wall friction coefficient and test the possible relationships between the granular temperature and the inertial number. Future progress in granular mechanics will require the challenging measure of granular temperature in experiments in order to tie the velocity and force fluctuations to the bed rheology.

5. Conclusion

Discrete element modeling of suspensions in air shows that athermal creeping at inertial number $<4 \times 10^{-5}$ is concurrent with an internal friction coefficient that is below the tangent of the angle of repose (static friction coefficient) of the mixture. Creeping of the flow also occurs at the flow-wall interface where stick-slick events induced by force fluctuations and particle rearrangement lead to nonzero average slip velocity on both flat frictional and rough substrates. On both types of surfaces, the wall friction coefficient at the flow base scales with a dimensionless slip that is the ratio of the slip velocity and rms velocity fluctuations and is independent of the air temperature and presence of excess pore pressure. On a flat frictional surface, the wall friction reaches a maximum for nondimensional slip > ~12 that corresponds to the wall-particle friction coefficient. On a rough substrate, the wall friction is maximum close to a nondimensional slip around unity and declines at large slip toward values close to that of the static friction coefficient. Given that the shear acted largely in planes parallel to the base, we investigated the scaling of the slip velocity with the shear rate and fluidity parameters. We show that a modified Navier slip law could be defined on a given roughness and imply that the shear rate scales with force fluctuations. Finally, we address the role of pore fluid pressure on the wall and internal friction coefficient of gas-particle and water-particle granular flows by defining of an effective wall and internal friction coefficients. These results suggest that the low effective friction coefficient required to simulate many geophysical mass flows is the result of a normal stress reduction not a wall friction reduction. Importantly, we show that the shear stress does not vanish in sheared fluidized bed even when the pore pressure equals the bed weight.

This work pushes forward our understanding of wall-friction and internal friction coefficient in gas-particle flows and helps to understand how wall and internal friction coefficient work in granular flows. This is particularly valuable to depth-averaged models that employ empirical friction coefficients to simulate geophysical mass flows.

In the future, it will be interesting to test these processes with aspherical particles, since the grain shape may influence the wall-slip interactions and associated scaling, and the role of polydispersity on the bed-substrate interactions and internal bed rheology. These avenues are currently being investigated by the authors.

Conflict of Interests

The authors declare no competing financial interests.

Data Availability Statement

The code used to produce the DEM-CFD is publicly available (http://mfix.netl.doe.gov). This work benefited from access to the University of Oregon High Performance Computer, Talapas. The data supporting the

conclusions are shown in the figures and tables presented. Interested readers will find additional data in the supporting information. On request the authors can also provide more specific results obtained from the experimental and numerical studies used to produce the figures. The data can be found at the Zenodo repository (https://zenodo.org/record/3832949).

References

Alonso, E. E., Zervos, A., & Pinyol, N. M. (2016). Thermo-poro-mechanical analysis of landslides: From creeping behaviour to catastrophic failure. *Géotechnique*, *66*(3), 202–219. https://doi.org/10.1680/jgeot.15.LM.006

Amarsid, L., Delenne, J. Y., Mutabaruka, P., Monerie, Y., Perales, F., & Radjai, F. (2017). Viscoinertial regime of immersed granular flows. *Physical Review E*, *96*(1), 012901. https://doi.org/10.1103/physreve.96.012901

Andreotti, B., Forterre, Y., & Pouliquen, O. (2013). *Granular Media: Between Fluid and Solid*. Cambridge: Cambridge University Press. https://doi.org/10.1017/CBO9781139541008

Artoni, R., & Richard, P. (2015). Effective wall friction in wall-bounded 3D dense granular flows. *Physical Review Letters*, *115*(15), 158001. https://doi.org/10.1103/PhysRevLett.115.158001

Barker, T., Schaeffer, D. G., Bohorquez, P., & Gray, J. M. N. T. (2015). Well-posed and ill-posed behaviour of the mu(I)-rheology for granular flow. *Journal of Fluid Mechanics*, *779*, 794–818. https://doi.org/10.1017/jfm.2015.412

Barker, T., Schaeffer, D. G., Shearer, M., & Gray, J. M. N. T. (2017). Well-posed continuum equations for granular flow with compressibility and $\mu(I)$-rheology. *Proceedings of the Royal Society A: Mathematical Physical and Engineering Science*, *473*(2201), 20160846. https://doi.org/10.1098/rspa.2016.0846

Benage, M. C., Dufek, J., & Mothes, P. A. (2016). Quantifying entrainment in pyroclastic density currents from the Tungurahua eruption, Ecuador: Integrating field proxies with numerical simulations. *Geophysical Research Letters*, *43*, 6932–6941. https://doi.org/10.1002/2016GL069527

Benyahia, S., Syamlal, M., & O'Brien, T. J. (2012). *Summary of MFIX Equations 2012–1*. Morgantown, WV: U.S. Department of Energy, National Energy Technology Laboratory. Retrieved from https://mfix.netl.doe.gov/documentation/MFIXEquations2012-1.pdf

Bergantz, G. W., Schleicher, J. M., & Burgisser, A. (2015). Open-system dynamics and mixing in magma mushes. *Nature Geoscience*, *8*(10), 793–796. https://doi.org/10.1038/ngeo2534

Bernard, J., Kelfoun, K., Le Pennec, J.-L., & Vallejo Vargas, S. (2014). Pyroclastic flow erosion and bulking processes; comparing field-based vs. modeling results at Tungurahua Volcano, Ecuador. *Bulletin of Volcanology*, *76*(9), 1–16. https://doi.org/10.1007/s00445-014-0858-y

Bernard, M., Climent, E., & Wachs, A. (2017). Controlling the quality of two-way Euler/Lagrange numerical modeling of bubbling and spouted fluidized beds dynamics. *Industrial & Engineering Chemistry Research*, *56*(1), 368–386. https://doi.org/10.1021/acs.iecr.6b03627

Berzi, D., & Vescovi, D. (2017). Shearing flows of frictionless spheres over bumpy planes: Slip velocity. *Computational Particle Mechanics*, *4*(4), 373–377. https://doi.org/10.1007/s40571-016-0115-6

Booth, A. M., Hurley, R., Lamb, M. P., & Andrade, J. E. (2014). Force chains as the link between particle and bulk friction angles in granular material. *Geophysical Research Letters*, *41*, 8862–8869. https://doi.org/10.1002/2014GL061981

Borykov, T., Mège, D., Mangeney, A., Richard, P., Gurgurewicz, J., & Lucas, A. (2019). Empirical investigation of friction weakening of terrestrial and Martian landslides using discrete element models. *Landslides*, *16*(6), 1121–1140. https://doi.org/10.1007/s10346-019-01140-8

Boyer, F., Guazzelli, É., & Pouliquen, O. (2011). Unifying suspension and granular rheology. *Physical Review Letters*, *107*(18), 188301. https://doi.org/10.1103/PhysRevLett.107.188301

Breard, E. C. P., Dufek, J., & Lube, G. (2017). Enhanced mobility in concentrated pyroclastic density currents: An examination of a self-fluidization mechanism. *Geophysical Research Letters*, *45*, 654–664. https://doi.org/10.1002/2017GL075759

Breard, E. C. P., Jones, J. R., Fullard, L., Lube, G., Davies, C., & Dufek, J. (2019). The permeability of volcanic mixtures—Implications for pyroclastic currents. *Journal of Geophysical Research: Solid Earth*, *124*, 1343–1360. https://doi.org/10.1029/2018JB016544

Campbell, C. S. (1989). Self-lubrication for long runout landslides. *Journal of Geology*, *97*(6), 653–665. https://doi.org/10.1086/629350

Carrara, A., Burgisser, A., & Bergantz, G. W. (2019). Lubrication effects on magmatic mush dynamics. *Journal of Volcanology and Geothermal Research*, *380*, 19–30. https://doi.org/10.1016/j.jvolgeores.2019.05.008

Charbonnier, S. J., Germa, A., Connor, C. B., Gertisser, R., Preece, K., Komorowski, J.-C., et al. (2013). Evaluation of the impact of the 2010 pyroclastic density currents at Merapi volcano from high-resolution satellite imagery, field investigations and numerical simulations. *Journal of Volcanology and Geothermal Research*, *261*, 295–315. https://doi.org/10.1016/j.jvolgeores.2012.12.021

Charbonnier, S. J., & Gertisser, R. (2009). Numerical simulations of block-and-ash flows using the Titan2D flow model: Examples from the 2006 eruption of Merapi Volcano, Java, Indonesia. *Bulletin of Volcanology*, *71*(8), 953–959.

Chialvo, S., & Sundaresan, S. (2013). A modified kinetic theory for frictional granular flows in dense and dilute regimes. *Physics of Fluids*, *25*(7), 070603. https://doi.org/10.1063/1.4812804

Cleary, P. W., & Campbell, C. S. (1993). Self-lubrication for long runout landslides: Examination by computer simulation. *Journal of Geophysical Research*, *98*(B12), 21,911–21,924. https://doi.org/10.1029/93JB02380

Collins, G. S., & Melosh, H. J. (2003). Acoustic fluidization and the extraordinary mobility of sturzstroms. *Journal of Geophysical Research*, *108*, 2473. https://doi.org/10.1029/2003JB002465

Corominas, J. (1996). The angle of reach as a mobility index for small and large landslides. *Canadian Geotechnical Journal*, *33*(2), 260–271. https://doi.org/10.1139/t96-005

Cosserat, E., & Cosserat, F. (1909). *Deformable Bodies*. Paris: Scientific Library a Hermann and Sons.

De Borst, R. (1991). Simulation of strain localization: A reappraisal of the Cosserat continuum. *Engineering Computations*, *8*, 317–332. https://doi.org/10.1108/eb023842

Druitt, T. H., Avard, G., Bruni, G., Lettieri, P., & Maez, F. (2007). Gas retention in fine-grained pyroclastic flow materials at high temperatures. *Bulletin of Volcanology*, *69*(8), 881–901. https://doi.org/10.1007/s00445-007-0116-7

Dufek, J., Wexler, J., & Manga, M. (2009). Transport capacity of pyroclastic density currents; experiments and models of substrate-flow interaction. *Journal of Geophysical Research*, *114*, B11203. https://doi.org/10.1029/2008JB006216

Erismann, T. H. (1979). Mechanisms of large landslides. *Rock Mechanics*, *12*(1), 15–46. https://doi.org/10.1007/bf01241087

Forterre, Y., & Pouliquen, O. (2008). Flows of dense granular media. *Annual Review of Fluid Mechanics*, *40*(1), 1–24. https://doi.org/10.1146/annurev.fluid.40.111406.102142

Fullard, L. A., Breard, E. C. P., Davies, C. E., Godfrey, A. J. R., Fukuoka, M., Wade, A., et al. (2019). The dynamics of granular flow from a silo with two symmetric openings. *Proceedings of the Royal Society A: Mathematical Physical and Engineering Sciences*, *475*(2221), 20180462. https://doi.org/10.1098/rspa.2018.0462

Gallier, S., Lemaire, E., Peters, F., & Lobry, L. (2014). Rheology of sheared suspensions of rough frictional particles. *Journal of Fluid Mechanics*, *757*, 514–549. https://doi.org/10.1017/jfm.2014.507

Garg, R., Galvin, J., Li, T., & Pannala, S. (2012). Open-source MFIX-DEM software for gas-solids flows: Part I—Verification studies. *Powder Technology*, *220*, 122–137. https://doi.org/10.1016/j.powtec.2011.09.019

GDR-MiDi (2004). On dense granular flows. *European Physical Journal E: Soft Matter and Biological Physics*, *14*, 341–365. https://doi.org/10.1140/epje/i2003-10153-0

Gidaspow, D. (1994). *Multiphase flow and fluidization: Continuum and kinetic theory description* (pp. 1–467). Academic Press.

Gesenhues, L., Camata, J. J., Côrtes, A. M. A., Rochinha, F. A., & Coutinho, A. L. G. A. (2019). Finite element simulation of complex dense granular flows using a well-posed regularization of the $\mu(I)$-rheology. *Computers & Fluids*, *188*, 102–113. https://doi.org/10.1016/j.compfluid.2019.05.012

Goldhirsch, I. (2010). Stress, stress asymmetry and couple stress: From discrete particles to continuous fields. *Granular Matter*, *12*(3), 239–252. https://doi.org/10.1007/s10035-010-0181-z

Goren, L., & Aharonov, E. (2007). Long runout landslides: The role of frictional heating and hydraulic diffusivity. *Geophysical Research Letters*, *34*, L07301. https://doi.org/10.1029/2006GL028895

Gu, Y., Ozel, A., & Sundaresan, S. (2016). Rheology of granular materials with size distributions across dense-flow regimes. *Powder Technology*, *295*, 322–329. https://doi.org/10.1016/j.powtec.2016.03.035

Hayashi, J. N., & Self, S. (1992). A comparison of pyroclastic flow and debris avalanche mobility. *Journal of Geophysical Research*, *97*(B6), 9063–9071. https://doi.org/10.1029/92JB00173

Henann, D. L., & Kamrin, K. (2013). A predictive, size-dependent continuum model for dense granular flows. *Proceedings of the National Academy of Sciences*, *110*(17), 6730. https://doi.org/10.1073/pnas.1219153110

Holyoake, A. J., & McElwaine, J. N. (2012). High-speed granular chute flows. *Journal of Fluid Mechanics*, *710*, 35–71. https://doi.org/10.1017/jfm.2012.331

Houssais, M., Ortiz, C. P., Durian, D. J., & Jerolmack, D. J. (2015). Onset of sediment transport is a continuous transition driven by fluid shear and granular creep. *Nature Communications*, *6*, 6527. https://doi.org/10.1038/ncomms7527

Houssais, M., Ortiz, C. P., Durian, D. J., & Jerolmack, D. J. (2016). Rheology of sediment transported by a laminar flow. *Physical Review E*, *94*(6–1). https://doi.org/10.1103/physreve.94.062609

Iverson, R. M. (2005). Regulation of landslide motion by dilatancy and pore pressure feedback. *Journal of Geophysical Research*, *110*, F02015. https://doi.org/10.1029/2004JF000268

Iverson, R. M., & George, D. L. (2014). A depth-averaged debris-flow model that includes the effects of evolving dilatancy. I. Physical basis. *Proceedings of the Royal Society A: Mathematical Physical and Engineering Sciences*, *470*(2170), 20130819. https://doi.org/10.1098/rspa.2013.0819

Iverson, R. M., Logan, M., LaHusen, R. G., & Berti, M. (2010). The perfect debris flow? Aggregated results from 28 large-scale experiments. *Journal of Geophysical Research*, *115*, F03005. https://doi.org/10.1029/2009JF001514

Iverson, R. M., Reid, M. E., & LaHusen, R. G. (1997). Debris-flow mobilization from landslides. *Annual Review of Earth and Planetary Sciences*, *25*(1), 85–138. https://doi.org/10.1146/annurev.earth.25.1.85

Iverson, R. M., Reid, M. E., Logan, M., LaHusen, R. G., Godt, J. W., & Griswold, J. P. (2010). Positive feedback and momentum growth during debris-flow entrainment of wet bed sediment. *Nature Geoscience*, *4*, 116. https://doi.org/10.1038/ngeo1040

Jenkins, J. T. (1992). Boundary conditions for rapid granular flow: Flat, frictional walls. *Journal of Applied Mechanics*, *59*(1), 120–127. https://doi.org/10.1115/1.2899416

Jenkins, J. T., & Berzi, D. (2010). Dense inclined flows of inelastic spheres: Tests of an extension of kinetic theory. *Granular Matter*, *12*(2), 151–158. https://doi.org/10.1007/s10035-010-0169-8

Jerolmack, D. J., & Daniels, K. E. (2019). Viewing Earth's surface as a soft-matter landscape. *Nature Reviews Physics*, *1*(12), 716–730. https://doi.org/10.1038/s42254-019-0111-x

Johnson, B. C., Campbell, C. S., & Melosh, H. J. (2016). The reduction of friction in long runout landslides as an emergent phenomenon. *Journal of Geophysical Research: Earth Surface*, *121*, 881–889. https://doi.org/10.1002/2015JF003751

Johson, P. C., & Jackson, R. (1987). Frictional-collisional constitutive relations for the granular materials, with application to plane shearing. *Journal of Fluid Mechanics*, *176*(1), 223–233. https://doi.org/10.1017/s0022112087000570

Jop, P., Forterre, Y., & Pouliquen, O. (2006). A constitutive law for dense granular flows. *Nature*, *441*, 727–730. https://doi.org/10.1038/nature04801

Kamrin, K. (2017). A hierarchy of granular continuum models: Why flowing grains are both simple and complex. *EPJ Web Conferences*, *140*, 01007. https://doi.org/10.1051/epjconf/201714001007

Kamrin, K., & Koval, G. (2012). Nonlocal constitutive relation for steady granular flow. *Physical Review Letters*, *108*(17), 178301. https://doi.org/10.1103/PhysRevLett.108.178301

Kean, J. W., Coe, J. A., Coviello, V., Smith, J. B., McCoy, S. W., & Arattano, M. (2015). Estimating rates of debris flow entrainment from ground vibrations. *Geophysical Research Letters*, *42*, 6365–6372. https://doi.org/10.1002/2015GL064811

Kelfoun, K. (2011). Suitability of simple rheological laws for the numerical simulation of dense pyroclastic flows and long-runout volcanic avalanches. *Journal of Geophysical Research*, *116*, B08209. https://doi.org/10.1029/2010JB007622

Legros, F. (2002). The mobility of long-runout landslides. *Engineering Geology*, *63*(3), 301–331. https://doi.org/10.1016/S0013-7952(01)00090-4

Li, T., Garg, R., Galvin, J., & Pannala, S. (2012). Open-source MFIX-DEM software for gas-solids flows: Part II—Validation studies. *Powder Technology*, *220*, 138–150. https://doi.org/10.1016/j.powtec.2011.09.020

Lube, G., Breard, E. C. P., Esposti-Ongaro, T., Dufek, J., & Brand, B. (2020). Multiphase flow behaviour and hazard prediction of pyroclastic density currents. *Nature Reviews Earth & Environment*, *1*(7), 348–365. https://doi.org/10.1038/s43017-020-0064-8

Lube, G., Breard, E. C. P., Jones, J., Fullard, L., Dufek, J., Cronin, S. J., & Wang, T. (2019). Generation of air lubrication within pyroclastic density currents. *Nature Geoscience*, *12*(5), 381–386. https://doi.org/10.1038/s41561-019-0338-2

Lucas, A., Mangeney, A., & Ampuero, J. P. (2014). Frictional velocity-weakening in landslides on Earth and on other planetary bodies. *Nature Communications*, *5*. https://doi.org/10.1038/ncomms4417

Lucchitta, B. K. (1987). Valles Marineris, Mars: Wet debris flows and ground ice. *Icarus*, *72*(2), 411–429. https://doi.org/10.1016/0019-1035(87)90183-7

Lun, C. K. K., Savage, S. B., Jeffrey, D. J., & Chepurniy, N. (1984). Kinetic theories for granular flow: Inelastic particles in Couette flow and slightly inelastic particles in a general flowfield. *Journal of Fluid Mechanics*, *140*, 223–256. https://doi.org/10.1017/S0022112084000586

Marzougui, D., Chareyre, B., & Chauchat, J. (2015). Microscopic origins of shear stress in dense fluid-grain mixtures. *Granular Matter*, *17*(3), 297–309. https://doi.org/10.1007/s10035-015-0560-6

Masson, D. G., Harbitz, C. B., Wynn, R. B., Pedersen, G., & Løvholt, F. (2006). Submarine landslides: Processes, triggers and hazard prediction. *Philosophical Transactions: Mathematical Physical and Engineering Sciences*, *364*(1845), 2009–2039. https://doi.org/10.1098/rsta.2006.1810

Melosh, H. J. (1979). Acoustic fluidization: A new geologic process? *Journal of Geophysical Research*, *84*(B13), 7513–7520. https://doi.org/10.1029/JB084iB13p07513

Ness, C., & Sun, J. (2015). Flow regime transitions in dense non-Brownian suspensions: Rheology, microstructural characterization, and constitutive modeling. *Physical Review E*, *91*(1), 012201. https://doi.org/10.1103/PhysRevE.91.012201

Ogburn, S. E., & Calder, E. S. (2017). The relative effectiveness of empirical and physical models for simulating the dense undercurrent of pyroclastic flows under different emplacement conditions. *Frontiers in Earth Science*, *5*, 83. https://doi.org/10.3389/feart.2017.00083

Ogburn, S. E., Calder, E. S., Cole, P. D., & Stinton, A. J. (2014). The effect of topography on ash-cloud surge generation and propagation. *Memoirs. Geological Society of London*, *39*, 179–194. https://doi.org/10.1144/M39.10

Pensa, A., Capra, L., Giordano, G., & Corrado, S. (2018). Emplacement temperature estimation of the 2015 dome collapse of Volcán de Colima as key proxy for flow dynamics of confined and unconfined pyroclastic density currents. *Journal of Volcanology and Geothermal Research*, *357*, 321–338. https://doi.org/10.1016/j.jvolgeores.2018.05.010

Pollock, N. M., Brand, B. D., Rowley, P. J., Sarocchi, D., & Sulpizio, R. (2019). Inferring pyroclastic density current flow conditions using syn-depositional sedimentary structures. *Bulletin of Volcanology*, *81*(8), 1–16. https://doi.org/10.1007/s00445-019-1303-z

Pouliquen, O. (2004). Velocity correlations in dense granular flows. *Physical Review Letters*, *93*(24), 248001. https://doi.org/10.1103/PhysRevLett.93.248001

Prancevic, J. P., & Lamb, M. P. (2015). Particle friction angles in steep mountain channels. *Journal of Geophysical Research: Earth Surface*, *120*, 242–259. https://doi.org/10.1002/2014JF003286

Pudasaini, S. P., & Miller, S. A. (2013). The hypermobility of huge landslides and avalanches. *Engineering Geology*, *157*, 124–132. https://doi.org/10.1016/j.enggeo.2013.01.012

Richman, M. W. (1988). Boundary conditions based upon a modified Maxwellian velocity distribution for flows of identical, smooth, nearly elastic spheres. *Acta Mechanica*, *75*(1), 227–240. https://doi.org/10.1007/BF01174637

Roche, O., Buesch, D. C., & Valentine, G. A. (2016). Slow-moving and far-travelled dense pyroclastic flows during the Peach Spring super-eruption. *Nature Communications*, *7*(1). https://doi.org/10.1038/ncomms10890

Roche, O., Nino, Y., Mangeney, A., Brand, B., Pollock, N., & Valentine, G. A. (2013). Dynamic pore-pressure variations induce substrate erosion by pyroclastic flows. *Geology*, *41*(10), 1107–1110.

Schaeffer, D. G., Barker, T., Tsuji, D., Gremaud, P., Shearer, M., & Gray, J. M. N. T. (2019). Constitutive relations for compressible granular flow in the inertial regime. *Journal of Fluid Mechanics*, *874*, 926–951. https://doi.org/10.1017/jfm.2019.476

Schneider, D., Bartelt, P., Caplan-Auerbach, J., Christen, M., Huggel, C., & McArdell, B. W. (2010). Insights into rock-ice avalanche dynamics by combined analysis of seismic recordings and a numerical avalanche model. *Journal of Geophysical Research*, *115*, F04026. https://doi.org/10.1029/2010JF001734

Shreve, R. L. (1968). The Blackhawk landslide. *Geological Society of America Special Paper*, *108*, 1–51.

Singer, K. N., McKinnon, W. B., Schenk, P. M., & Moore, J. M. (2012). Massive ice avalanches on Iapetus mobilized by friction reduction during flash heating. *Nature Geoscience*, *5*, 574. https://doi.org/10.1038/ngeo1526

Staron, L. (2008). Correlated motion in the bulk of dense granular flows. *Physical Review E*, *77*(5), 051304. https://doi.org/10.1103/PhysRevE.77.051304

Syamlal, M. (1998). *MFIX documentation: Numerical technique, DOE/MC/31346-5824, DE98002029* (pp. 1–80). Washington, DC: U.S. Department of Energy.

Syamlal, M., Musser, J., & Dietiker, J.-F. (2016). The two-fluid model in MFIX. In E. E. Michaelides, C. T. Crowe, J. D. Schwarzkopf (Eds.), *Multiphase Flow Handbook* (2nd ed. pp. 242–274). Boca Raton, Florida, USA: CRC Press.

Trolese, M., Giordano, G., Komorowski, J. C., Jenkins, S. F., Baxter, P. J., Cholik, N., et al. (2018). Very rapid cooling of the energetic pyroclastic density currents associated with the 5 November 2010 Merapi eruption (Indonesia). *Journal of Volcanology and Geothermal Research*, *358*, 1–12. https://doi.org/10.1016/j.jvolgeores.2018.06.004

Urlaub, M., Talling, P. J., Zervos, A., & Masson, D. (2015). What causes large submarine landslides on low gradient (<2°) continental slopes with slow (∼0.15 m/kyr) sediment accumulation? *Journal of Geophysical Research: Solid Earth*, *120*, 6722–6739. https://doi.org/10.1002/2015JB012347

Vardoulakis, I. (2000). Catastrophic landslides due to frictional heating of the failure plane. *Mechanics of Cohesive-frictional Materials*, *5*(6), 443–467. https://doi.org/10.1002/1099-1484(200008)5:6<443::aid-cfm104>3.0.co;2-w

Voight, B., & Faust, C. (1982). Frictional heat and strength loss in some rapid landslides. *Géotechnique*, *32*(1), 43–54. https://doi.org/10.1680/geot.1982.32.1.43

Wang, Y. F., Dong, J. J., & Cheng, Q. G. (2017). Velocity-dependent frictional weakening of large rock avalanche basal facies: Implications for rock avalanche hypermobility? *Journal of Geophysical Research: Solid Earth*, *122*, 1648–1676. https://doi.org/10.1002/2016JB013624

Weinhart, T., Hartkamp, R., Thornton, A. R., & Luding, S. (2013). Coarse-grained local and objective continuum description of three-dimensional granular flows down an inclined surface. *Physics of Fluids*, *25*(7), 070605. https://doi.org/10.1063/1.4812809

Weinhart, T., Labra, C., Luding, S., & Ooi, J. Y. (2016). Influence of coarse-graining parameters on the analysis of DEM simulations of silo flow. *Powder Technology*, *293*, 138–148. https://doi.org/10.1016/j.powtec.2015.11.052

Wilson, C. J. N. (1980). The role of fluidization in the emplacement of pyroclastic flows: An experimental approach. *Journal of Volcanology and Geothermal Research*, *8*, 231–249. https://doi.org/10.1016/0377-0273(80)90106-7

Zhang, Q., & Kamrin, K. (2017). Microscopic description of the granular fluidity field in nonlocal flow modeling. *Physical Review Letters*, *118*(5), 058001. https://doi.org/10.1103/PhysRevLett.118.058001